TECHNISCHE UNIVERSITÄT WIEN
Vienna University of Technology

DIPLOMARBEIT

# On the use of the Doppler centroid anomaly for the detection of water bodies under the severe wind conditions.

Ausgeführt am Department
für Geodäsie und Geoinformation,
Forschungsgruppe Fernerkundung,
der Technischen Universität Wien

unter der Anleitung von
Univ.Prof. Dipl.-Ing. Dr.techn. Wolfgang Wagner

durch
Bc. Alena Dostálová

Matr.-Nr.: 1028873
Mendlova 3, 69003 Břeclav
Tschechien

Wien, September 2014 ______________________

# Abstract

Over the last years, methods for automated retrieval of the water bodies and flooded areas from Synthetic Aperture Radar (SAR) satellite data are an important research topic. However, most of these methods have restrictions over rough water surfaces caused by high wind conditions. Therefore there is the need for method that could work also over roughened water surface. One possibility could be the use of other information that is available from the SAR data apart from the traditionally used normalized radar cross-section (NRCS) images.

One of the ancillary datasets delivered along the Envisat Advanced Synthetic Aperture Radar (ASAR) Wide Swath (WS) mode data is a measured Doppler centroid value. The Doppler centroid value is dependent on a relative speed of the satellite and Earth surface towards or from each other. With the knowledge of satellite orbit and attitudes and Earth rotation speed, the theoretical, modelled, Doppler centroid values may be computed. For a stable Earth surface, the difference between these two values (Doppler centroid anomaly) should be close to 0, whereas for the moving surface, such as water surface influenced by surface currents and winds, the anomaly should be dependent on the relative speed of the water surface in the perpendicular direction to the satellite orbit track.

The radial surface velocities based on the Doppler centroid anomalies have already been successfully used for retrieving wind speed and direction over the oceans as well as a usefulness for the studies of ocean currents has been investigated. In this Thesis, the use of the radial surface velocity for detection of inland water surfaces is studied – whether the inland water surfaces are detectable in the Doppler centroid anomaly data and what the limitations of this method are.

Although the relationship between wind speed in the radar line of sight direction and radial surface velocity data was confirmed also for inland water pixels (Pearson correlation coefficient of 0.79), the currently available ASAR WS radial surface velocity data were found unsuitable for the inland water mapping. The main limitations are very coarse spatial resolution and low retrieval accuracy, especially in densely urbanized areas. However, both the spatial resolution and retrieval accuracy are expected to improve in case of the radial surface velocity data derived from the recently launched Sentinel-1 satellite.

# Acknowledgements

The presented research was undertaken at the Research Group Remote Sensing within the Department of Geodesy and Geoinformation at Vienna University of Technology. I would like express my greatest gratitude to my colleagues for providing such a great working environment and atmosphere and for their help during the process of writing this thesis. A special thanks goes to my supervisor Prof. Wolfgang Wagner, for his support and encouragement up to this day.

I would like to thank the Nansen Environmental and Remote Sensing Center in Norway for their support with the data processing in the early stages of this Thesis and especially to Dr. Morten W. Hansen who provided me with the radial surface velocity data. Without their help, this work would not be possible.

I would also like to express my gratitude to Marcela Doubková for her useful comments and substantial support especially during the last months of the work. Her insights contributed significantly to the quality of this Thesis.

Finally, I would like to thank my family and friends for their continuous support and patience from the beginning to the end of this Master Thesis.

# Table of contents

# List of Figures

# List of Tables

# Acronyms

| | |
|---|---|
| ALOS | Advanced Land Observation Satellite |
| AP | Alternating Polarisation |
| ASAR | Advanced Synthetic Aperture Radar |
| ASCAT | Advanced Scatterometer |
| DEM | Digital Elevation Model |
| DORIS | Doppler Orbitography and Radiopositioning Integrated by Satellite |
| ECMWF | European Centre for Medium-Range Weather Forecasts |
| Envisat | Environmental Satellite |
| ERS | European Remote-Sensing |
| ESA | European Space Agency |
| GM | Global Monitoring |
| GMF | Geophysical Mapping Function |
| IEEE | Institute of Electrical and Electronics Engineers |
| IM | Image Mode |
| IRS | Indian Remote-Sensing Satellite |
| LISS | Linear Imaging Self-Scanner |
| MetOp | Meteorological Operational Platform |
| NERSC | Nansen Environmental and Remote Sensing Center |
| NEST | Next ESA SAR Toolbox |
| NRCS | Normalized Radar Cross-Section |
| PALSAR | Phased Array type L-Band Synthetic Aperture Radar |
| QuickSCAT | Quick Scatterometer |
| RAR | Real Aperture Radars |
| RMSE | Root Mean Square Error |
| SAR | Synthetic Aperture Radar |
| SNR | Signal-to-Noise Ratio |
| SPOT | Satellite for observation of Earth |
| SRTM | Shuttle Radar Topography Mission |
| WMO | World Meteorological Organisation |
| WS | Wide Swath |
| WV | Wave Mode |

# Chapter 1

## Introduction

With the rapid growth of the Earth population and an increasing demand of water for agriculture, industry or for supply of the urban areas, the precise knowledge of the available water storage becomes increasingly important. This importance is further enhanced by the ratio of fresh (3%) and saline water (97 %) and by the fact that most of the fresh water is stored in form of icecaps, glaciers and ground water. Only a small fraction of the available water is stored in its liquid form in rivers, reservoirs and lakes (Gleick, 1996). Precise and up-to-date knowledge of the distribution of the available fresh water storage contributes towards a better understanding of interactions between the global climate system and water cycle, human impacts on water resources as well as towards the improvement of the hydrological models and initialisation of water resources forecasts (Van Dijk et al.,2014)

Satellite remote sensing plays a major role in the monitoring of surface waters. A variety of optical, thermal as well as radar systems is used to locate the surface water and specify the water extent in permanent water bodies such as seas, oceans, rivers and lakes as well as in temporary water bodies such as flooded regions or intermittent lakes. Each measurement approach has its advantages as well as disadvantages when compared to the others. According to Schultz and Engman (2000), the delineation of the water surface can be most easily performed using the near-infrared and visible wavelengths. This is due to a very different reflectance and absorption values for water when compared to the bare soil and vegetation - water absorbs most of the energy in the near and middle infrared wavelengths, reflecting only a small fraction of incoming energy, whereas the reflectance of soil and vegetation is much higher for these bands. As a result, there is a strong contrast between water and land surfaces in the infrared or multi-spectral images.

However, the optical data are limited to the ideal observation conditions. The most important constraint of regular temporal coverage is the need for cloud free conditions. Also the need of the sun illumination limits the usable acquisition times only to the day-time observations. This becomes crucial when frequent measurements of an area are needed. Especially in case of flood monitoring, cloud contamination is often a limiting factor for usage of the satellite imagery in visible and thermal domain.

These limitations can be circumvented by using the sensors in the microwave domain (frequencies ranging approximately from 0.3 to 300 GHz). Microwaves are not only independent on the illumination of the surface and therefore capable of both day and night acquisitions, but can also penetrate clouds and, to some extent, also rain. With the improving spatial resolution of available synthetic aperture radar (SAR) sensors, microwave remote sensing becomes increasingly important for water surface mapping.

The techniques used for the mapping of the water surfaces with the help of SAR sensors are typically based on the characteristic microwave signal response on the calm water surface - due to relatively low roughness of water surface, most of the radar signal is reflected away from the sensor (specular reflection), whereas over land, surface roughness and potentially also vegetation cause more complex reflection. As a result, water surface appears to be dark when compared to other land surfaces. An example is shown in Figure 1-1 (a), where the water surface of the Balaton Lake in Hungary is clearly distinguishable from the surrounding land due to their low backscatter values. The histogram of the backscatter values of land (green) and water (blue) pixels shows clear boundary between the two classes at a threshold of about -14 dB.

This assumption has, however, some limitations. There may e.g. be Bragg resonance effects that cause enhanced radar backscatter over rough water surfaces (Schultz and Engman, 2000). Generally, with the increasing wind speed over water bodies, the measured backscatter also increases and water can be misinterpreted as land surface. An example is shown in Figure 1-1 (b) which shows the same scene as the Figure 1-1 (a) but in windy conditions. The backscatter values over water and land surface are overlapping and the water can no longer be distinguished from land pixels.

Furthermore, many land surfaces appear to be smooth to microwave and can be misinterpreted as a water surface. These include artificial surfaces such as roads or airports or naturally smooth surfaces, such as sand deserts. These limitations hamper the delineation of the water extent, especially when using only single SAR images.

a)

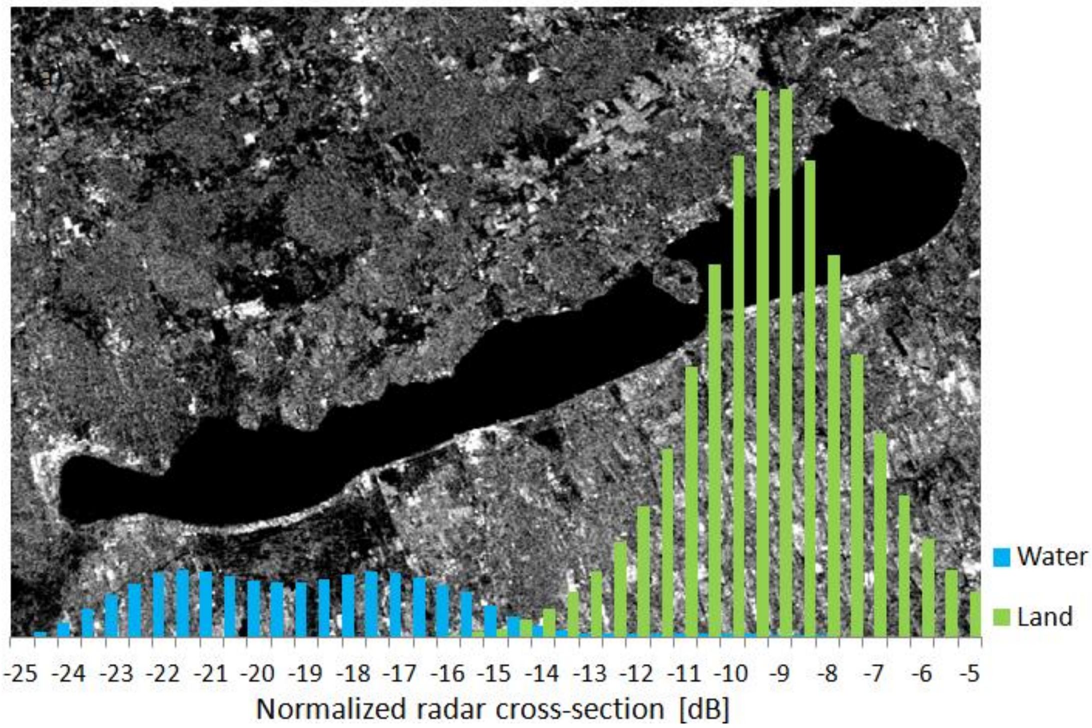


b)

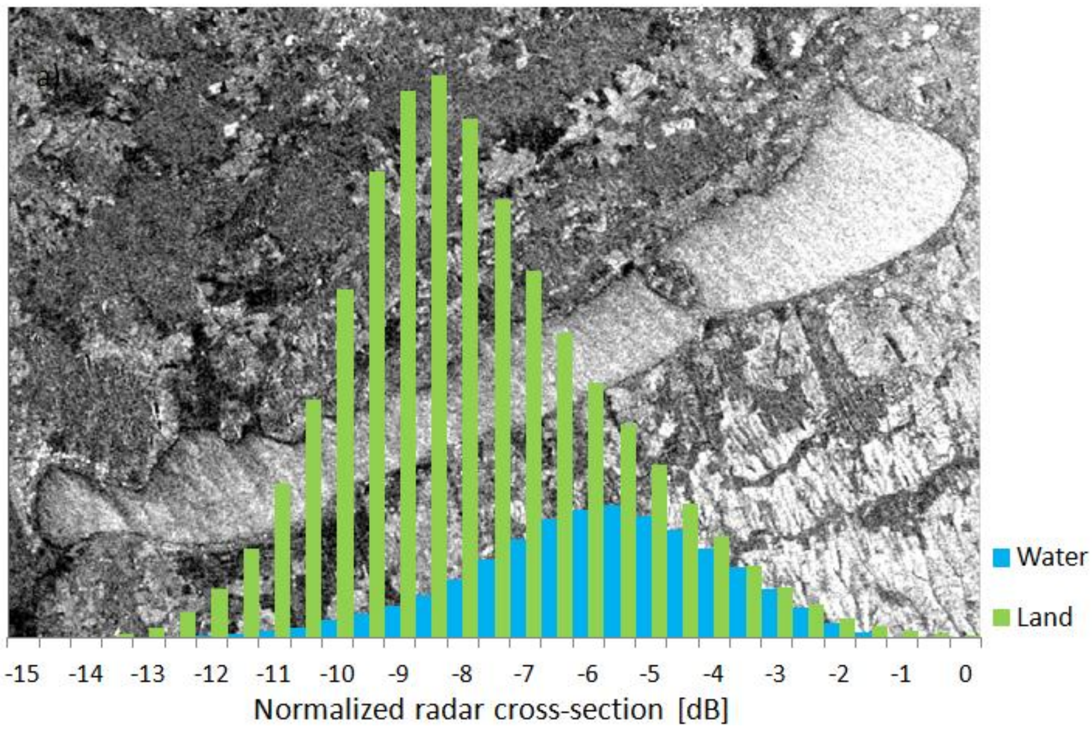


Figure 1-1: Histograms of NRCS values for land and water area for surroundings of Balaton Lake. a) 17$^{th}$ October 2009; 20:34:15, b) 14$^{th}$ October 2009; 09:07:14.

Apart from the traditionally used normalized radar cross-section (NRCS) the SAR data contain also the so-called Doppler centroid anomaly that was recently tested and used for the SAR based wind speed and direction retrieval over the ocean surfaces (Mouche et al., 2012). The Doppler centroid anomalies are computed as the difference between the theoretically modelled and actually measured Doppler centroid values. This difference can be converted into the relative radial surface velocities describing the relative motion between the Earth surface and the sensor in the sensor view direction. According to the theory, the Doppler centroid anomaly and therefore also the relative radial surface velocity is equal or very close to zero for any stable Earth surface. In case of an additional movement of the surface away or towards the sensor apart from the Earth rotation, this movement will be reflected in the Doppler centroid anomaly value. Positive values indicate the targets receding from the radar and negative those approaching the radar. As such, the Doppler centroid anomaly detects also the motion of the water surface caused by the currents and winds over the water. In SAR oceanography, the radial surface velocity was successfully used to complement the NRCS information from SAR to retrieve both wind speed and direction (Mouche et al., 2012., Wang et al., 2014, Johannessen et al., 2014). It can be expected that a similar behaviour is also observable over inland water bodies. If so, the Doppler centroid anomaly could be used to complement the backscatter values to distinguish the water surfaces from the surrounding land surface in case of severe wind conditions.

The strongest limitation of this approach is much lower spatial resolution of the today available Doppler centroid anomaly datasets when compared to the original NRCS images. The estimation accuracy of the Doppler centroid data is dependent on the estimation block size and the backscatter variation within this block (Chapron et al., 2005). To obtain accurate Doppler centroid estimates, sufficiently large estimation blocks are needed. In case of the Environmental Satellite (Envisat) Advanced Synthetic Aperture Radar (ASAR) Wide Swath (WS) mode data the spatial resolution of the auxiliary Doppler centroid data ranges between 3.5 km in far range and 9 km in near range in range direction (perpendicular to the flight direction) and is fixed to approximately 8 km in azimuth direction (parallel to the flight direction). This compares to the 150 m spatial resolution in both directions in NRCS image. The dataset with spatial resolution in order of several kilometres is not suitable for water bodies mapping by itself. Given, however, that the Doppler centroid anomaly is derived from the identical SAR dataset as the NRCS image and reflects the water surface movement caused by the severe wind conditions, it might complement the high resolution backscatter information in case that the strong wind and water currents increase the NRCS values over the water surface and the water surface mapping using only NRCS values fails. Furthermore, the spatial resolution is expected to be improved in newer SAR missions such as the recently launched Sentinel 1 mission. For instance, the Sentinel 1 mission will contain the radial surface velocity data with a spatial resolution of 1 km and improved retrieval accuracy as a part of the Level 2 ocean product (Engen & Johnsen, 2010).

The objective of this thesis is to evaluate the possibility and limitations of the usage of the radial surface velocity information from the available Envisat ASAR WS mode data for the inland water bodies' detection with an outlook to the European Space Agency (ESA) Sentinel 1 mission. The

Doppler centroid anomaly data has so far been used only in the SAR oceanography, but it's usability over land water bodies was not yet evaluated.

Due to the very low spatial resolution of the Doppler centroid anomaly dataset, the study focused on the lakes with an area of at least 300 km squared. Such large lakes are covered with at least 6 pixels of the Doppler centroid anomaly image (under the assumption that the average Doppler centroid pixel has an area of 6 by 8 km). It should be noted that the objective of this work is not to provide a method for lake detection that would replace the existing methods from NRCS imageries; especially because it is no challenge to map water surface of such an extent with the help of NRCS data. The objective is to evaluate the possibility of usage of the Doppler centroid anomaly from future sensors with an improved spatial resolution that could potentially complement existing methods from NRCS imageries especially under windy conditions.

The structure of the work is as follows: Chapter 2 explains the basics of the SAR and introduces the Envisat ASAR sensor and data used in the thesis. Chapter 3 describes the state-of-the-art methods for the mapping of water surfaces with the help of SAR and summarizes their limitations. Chapter 4 gives a short introduction into the wind measurements over the ocean using SAR and explains theoretically how to compute the radial surface velocity from the SAR data. Chapter 5 summarises all processed data used in this thesis and the methodology. Chapter 6 describes the results of this feasibility study. Finally, the summary and outlook to the Sentinel-1 mission is provided in chapter 7.

# Chapter 2

# Synthetic aperture radar

## 2.1 Theoretical background

Microwave remote sensing sensors use the electromagnetic radiation within the microwave frequency range to acquire the information about the Earth surface and atmosphere. The microwave portion of the electromagnetic wave spectra covers the range of frequencies between approximately 0.3 and 300 GHz, although no firm definition of these limits exists. The spectrum is typically further divided into a number of classes named by letters. Multiple classifications exist. As an example Table 2-1 shows the band classification according to the Institute of Electrical and Electronics Engineers (IEEE) standard number 521-1984.

| Band designator | Frequency range [GHz] | Wavelength [cm] |
|---|---|---|
| **L** | 1 - 2 | 30.00 - 15.00 |
| **S** | 2 - 4 | 15.00 - 7.50 |
| **C** | 4 - 8 | 7.50 - 3.80 |
| **X** | 8 - 12 | 3.80 - 2.50 |
| **Ku** | 12 - 18 | 2.50 - 1.70 |
| **K** | 18 - 27 | 1.70 - 1.10 |
| **Ka** | 27 - 40 | 1.10 - 0.75 |
| **V** | 40 - 75 | 0.75 - 0.40 |
| **W** | 75 - 110 | 0.40 - 0.27 |

Table 2-1: The band classification according to the IEEE standard number 521-1984

Based on their measuring principle, microwave remote sensing sensors are commonly divided in two groups - active and passive. The passive sensors (radiometers) detect the natural emission of the Earth surface in the specified frequency, whereas the active instruments (such as Scatterometers and Synthetic Aperture Radars) work as both detectors and transmitters. The signal with specific properties (frequency, polarisation) is transmitted from the antenna towards the Earth surface where it is scattered depending on the geometric and dielectric properties of the surface, observation geometry as well as on the signal frequency and polarisation. The ratio between the transmitted and received signal is traditionally expressed as normalized radar cross-section (NRCS).

Three main resolution types are commonly used to characterise the microwave remote sensing instruments: spatial, temporal and radiometric resolution. Spatial resolution is a measure of the smallest object that can be resolved by the sensor. Temporal resolution describes how often the sensor can acquire observations of a specified area of interest. Radiometric resolution determines the smallest change in received signal that can be detected by the sensor.

The spatial resolution of the side looking radar system is defined in two perpendicular dimensions; range direction, meaning the direction perpendicular to the satellite orbit or flight track and azimuth direction parallel to the orbit (see Figure 2-1).

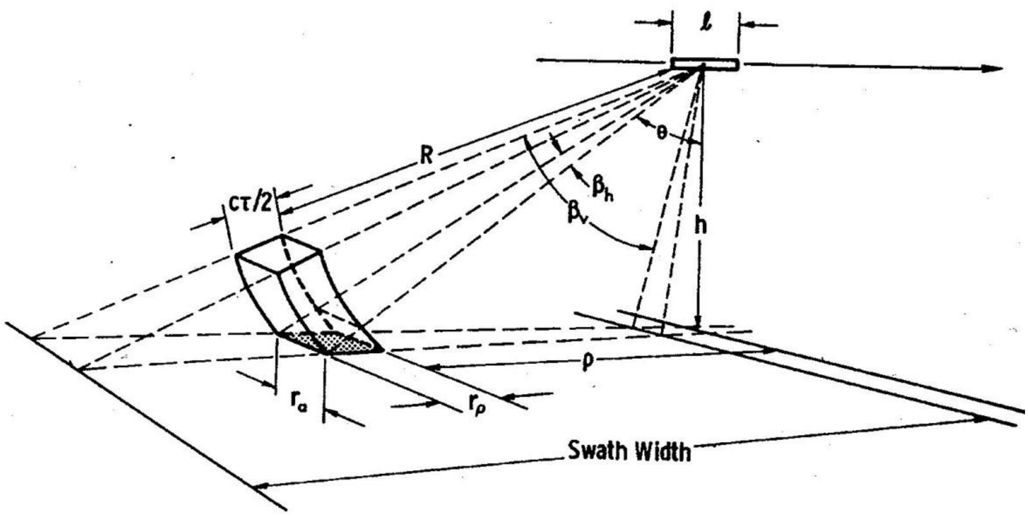


Figure 2-1: Geometry of the side-looking radar. Source: Ulaby et al., 1982

Generally the spatial resolution in range direction is dependent on the length of the signal pulse - the shorter the pulse duration, the better the spatial resolution. On the other hand, shorter pulse length decreases the signal-to-noise ratio (SNR) and hence the radiometric resolution of the returned signal. Therefore, pulse compression techniques applied on the longer pulses are commonly employed to preserve high SNR as well as high spatial resolution (Curlander & McDonough, 1991).

The spatial resolution in the azimuth direction is dependent on the wavelength of the signal and size of the antenna in the along-track direction as shown in equation 2.1.

$$r_a = \frac{h\lambda}{l sin(\gamma)} \quad (2.1)$$

where:

$r_a$ ... spatial resolution in azimuth direction

$h$ ... height of the sensor above Earth surface

$l$ ... size of the antenna in the along-track direction

$\gamma$ ... depression angle (angle between radar line of sight and horizontal plane)

$\lambda$ ... wavelength

Hence, to get higher spatial resolution in azimuth direction when using the same frequency, larger antenna is needed. In the space borne microwave domain (wavelengths approximately in the range of 1 mm to 1 m and orbiting heights around 800 km) this is an important limiting factor for the sensor resolution. The so-called real aperture radars (RAR) (such as Meteorological Operational Platform (MeTop)-A and B Advanced Scatterometer (ASCAT) or Quick Scatterometer (QuickSCAT) SeaWinds scatterometers) are therefore limited to the spatial resolutions of around 25 km.

To overcome this limitation, one large antenna can be simulated by many small antennas. The variation of the relative phases of the signals feeding the antennas is used in such way that the constructive and destructive interference reinforces the effective radiation pattern of the resulting phased array antenna in the desired direction. The concept of the array of real antennas can also be substituted by a single antenna mounted on a moving platform (Figure 2-2). An important precondition is the coherency of the transmitted signal - as long as both the amplitude and a phase of a received signal is recorded the single moving antenna is equivalent to the array of antennas. Such technique is generally referred to as Synthetic Aperture Radar (SAR).

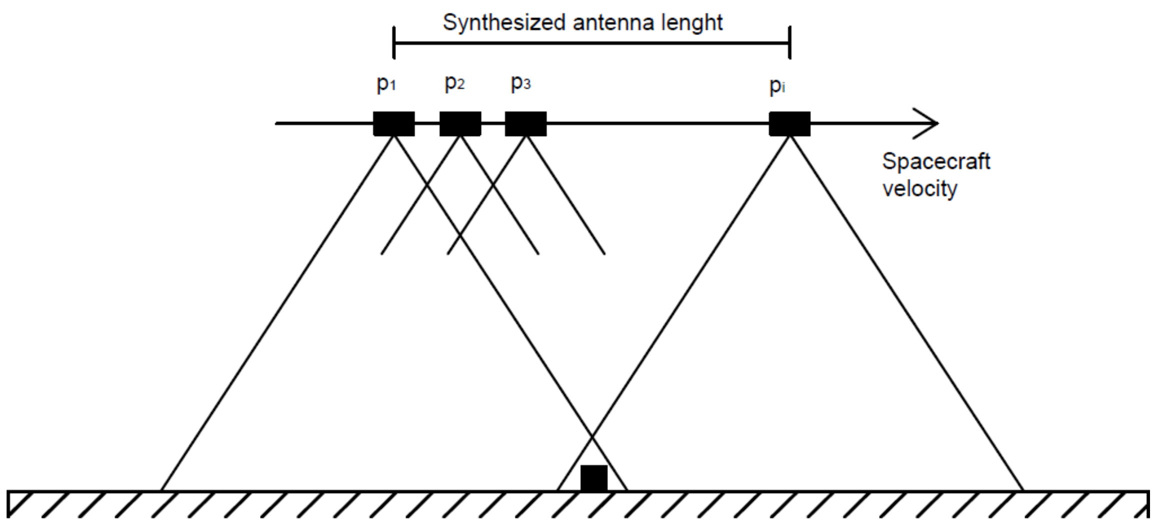


Figure 2-2: The principle of synthesized long antenna created by overpass of one moving antenna.

The SAR technique uses the Doppler effect that describes the change of the frequency of the electromagnetic wave as a function of the wavelength and the relative speed between the transmitter and the receiver:

$$f_D = \frac{V_{rel}}{\lambda} \tag{2.2}$$

where:

$f_D$ ... Doppler shift in frequency

$V_{rel}$ ... relative speed between the transmitter and receiver

When the transmitter approaches the receiver, the signal is compressed, causing a decrease of wavelength and an increase of frequency. When the transmitter recedes from the receiver, the opposite applies.

As the satellite overpasses, the target stays within its footprint for a longer period of time. The slant range between the target and the sensor changes continuously. It is getting shorter as the satellite approaches and longer as the satellite recedes. This causes the continuous changes of the frequency. Taking into consideration the change in the slant range, also the phase of the received signal differs as the satellite overpasses. By recording and analysing the phase history, it is possible to determine from which part of the beam the echo returns.

The range of observable Doppler frequencies (Doppler bandwidth) is dependent on the size of the radar footprint. When reducing the antenna size, the footprint of the instrument increases, causing also wider spread of available Doppler frequencies. The azimuthal resolution of a SAR system is determined by the Doppler bandwidth as in:

$$r_a = \frac{V_s}{B_D} = \frac{V_s \lambda 2D}{4V_s \lambda} = \frac{D}{2} \tag{2.3}$$

where:

$V_S$ ... relative velocity

$B_D$ ... Doppler bandwidth

D ... real antenna length

On the contrary to the RAR (equation 2.1), the azimuthal resolution of a SAR system actually increases with the decreasing real antenna size (equation 2.3). Using the synthesized large antenna, the SAR systems are capable of achieving the azimuthal spatial resolution equal to half of the real antenna size. Furthermore, this value is independent on radar wavelength and orbital height (Raney, 1986).

Fine spatial resolution in order of meters to hundreds of meters is the main objective of the SAR systems. This comes at the expense of temporal and radiometric resolution as well as geographic coverage of these sensors when compared to the scatterometers. However, numerous applications - such as water bodies monitoring, flood monitoring or regional monitoring of soil moisture or freeze and thaw require spatial resolution equal or even better that that of current SAR systems. Depending on the intended application, the SAR systems use a variety of acquisition modes representing various combinations of the spatial and radiometric resolution and ground coverage.

## 2.2 Doppler parameters

When processing the raw SAR images into the Level 1b product, three steps are applied (Envisat ASAR product Handbook, 2007):

- Pre-processing: ingest and correct the raw data
- Doppler centroid estimation
- Image formation: process the raw data into an image

As the Doppler centroid data are used in this work to derive the Doppler centroid anomaly and thus the radial surface velocity dataset, the second processing step requires a thorough explanation.

The Doppler centroid frequency of the SAR signal corresponds to the Doppler shift of a target positioned in the centre of the antenna beam. It is one of the key input parameters in the processing of SAR imagery (Hansen et al., 2011). Errors in the Doppler centroid frequency estimation causes a degradation of the processing performance and image quality. More precisely, erroneous Doppler centroid values leads to a degradation of the SNR, higher azimuth ambiguity level and an azimuth shift of the pixel (Li et al., 1985, Madsen et al., 1989). The azimuth ambiguities appear in the SAR image as so-called ghost targets inside low reflectivity area (such as water surface) caused by the displacement of high reflectivity objects (such as urban areas) located in the azimuth direction.

The Doppler centroid varies with both range and azimuth and there are two possibilities, how to estimate the centroid values:

- to model the Doppler centroid using the information about the satellite trajectory and instrument attitudes
- to directly analyse the received complex echo data

The first possibility requires very precise information about the attitudes (orientation) of the sensor as well as accurate orbital parameters computed from the tracking data. Any uncertainties in these parameters will result in an erroneous Doppler centroid. Moreover, the time lag in smoothing and refining of the tracking data may make this method inconvenient. While the spacecraft attitudes are generally accurate enough to ensure the precise Doppler parameters values, the time lag of the precise orbit availability remain problematic, especially when the real time processing is required. For the above reasons, most processors of the SAR data contain procedures for automatic Doppler centroid detection from the radar data itself (Curlander & McDonough, 1991).

A common technique for the Doppler centroid estimation from the coherent SAR uses the azimuth power spectra of the SAR data. In general, this spectrum exhibits a pattern that is similar to the antenna power pattern and the Doppler centroid parameters can be extracted by searching for the maximum of this spectrum (Li et al., 1985). Nowadays, various algorithms exists. The Doppler centroid anomaly and relative radial surface velocity estimation is discussed in detail in chapter 4.

## 2.3 Envisat ASAR

For the purpose of this thesis, the SAR data from ESA Envisat ASAR sensor were used due to the availability of the gridded Doppler centroid dataset as a part of the Wide Swath (WS) mode product. The Envisat satellite was launched in 2002 by ESA as a successor of the European Remote-Sensing (ERS) satellites. The mission was originally planned for 5 years, but was extended until 8$^{th}$ April 2012 when the connection to the satellite was lost. It carried 10 different earth observation instruments onboard, including the Advanced Synthetic Aperture Radar (ASAR). The ASAR instrument provided C-Band microwave measurements with a central frequency of 5.331 GHz in variety of measurement modes. Generally, these could be divided into global mission modes including Global Monitoring Mode (GM) and Wave Mode (WV) and regional mission modes including Image Mode (IM), Alternating Polarisation Mode (AP) and WS Mode. The spatial resolution ranges between 30 m in case of the IM or AP modes and 1 km in case of the GM mode. The orbit repeat cycle is 35 days. The temporal resolution is dependent on the measurement mode and the acquisition plan of the satellite and is therefore quite variable. Over the land, the Global Monitoring Mode provides most frequent measurements; up to 2 acquisitions a week in some areas. The technical characteristics of the Envisat satellite are summarized in Table 2-2.

| | |
|---|---|
| **Repeat cycle** | 35 days |
| **Orbit period** | 100.59 min |
| **Mean local solar time at descending node** | 10:00 |
| **Inclination** | 98.55 deg |
| **Orbit velocity** | 7.45 km/s |
| **Semi Major Axis** | 7159.5km |
| **Frequency** | 5.331 GHz (C-Band) |
| **Lifetime** | 1st March 2002 - 8th April 2012 |

Table 2-2: Envisat ASAR - technical characteristics

For the purpose of this thesis, the Level 1b WS mode images were used. WS mode is one of the scanning SAR (ScanSAR) modes of the Envisat ASAR instrument. Enhanced swath width of 405 km is achieved by utilising the electronic steering of antenna beam in elevation. The operation time is shared between several parallel sub-swaths in the along-flight direction. The sensor transmits pulses to, and receives echo from, each single sub-swath for the time long enough to synthesise the radar image of the desired resolution before it switches to the next sub-swath. The WS mode is comprised of 5 sub-swaths as shown in Figure 2-3, enhancing significantly the geographical coverage and thus shortening the satellite revisit time. The spatial resolution of the WS mode is equal to 150 m both in azimuth and in range direction with pixel spacing of 75m. The WS measures in both HH or in VV polarisation (Envisat ASAR product Handbook, 2007).

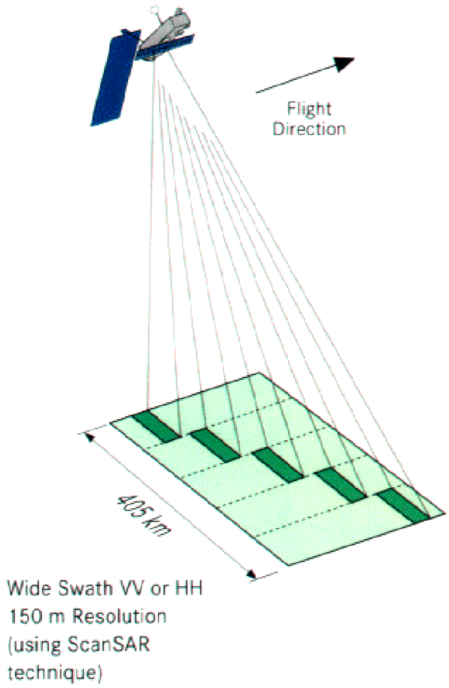


Figure 2- 1: The Envisat ASAR Wide Swath Mode. Source: Envisat ASAR product Handbook, 2007.

The WS mode is traditionally used for the water surface detection, because of the combination of relatively high spatial and temporal resolution. Importantly, the gridded Doppler centroid information is available as an auxiliary dataset within the WS mode data since 2007.

# Chapter 3

## SAR-based water surface mapping

### 3.1 State-of-the-art

SAR instruments are well suited for the water surface detection, since they combine the relatively high spatial resolution with the potential of practically all-weather observation capabilities. Traditionally, the NRCS images are used. Multiple methods exist that aim to monitor the water surface with the help of the SAR observations. Generally, all of these methods exploit the fact that the water surface has lower backscatter intensities when compared to other land classes. Although intensive research is dedicated to fully automated approaches that would map the water surface globally, most of the existing methods require some kind of manual interaction.

The existing methods can be divided in two main classes: object-based and pixel-based methods. Whereas the conventional pixel-based approach operates on pixel basis, as the smallest components of the raster images, the object based methods analyse image objects or segments. These objects are created based on similarity criteria of grey values or textural properties (Hahmann et al., 2008).

Some methods require single image scene while others rely on the multi-temporal analyses. Especially the permanent water bodies' mapping benefits from the use of multiple SAR imageries. The effects of wind and currents can be eliminated by averaging or filtering of longer time series of the data. Also in case of the flood mapping, the multi-temporal analysis has been proven superior to the single image approaches (Hahmann et al., 2008). These include various change detection methods comparing the acquisition of a flooded area with a non-flooded reference dataset of the same area.

Among the single image approaches, the so-called histogram thresholding methods (i.e. Bates et al., 1997) represent one of the most common approaches for the water surface detection. These have been used with some alternations in many different works (Matgen et al., 2011). Generally, the image is divided in two classes - water and non-water - based on a threshold value for radar cross-section. This value may be manually selected for each individual image, or found with the help of an automated algorithm such as an Otsu method (Otsu, 1979). As a result, all image pixels with a lower value than the specified threshold will be classified as water.

The requirements of this approach include a high contrast between the water and land area and coverage of the water surface that must cover sufficient number of water pixels. Ideally, the histogram should be a mixture of two clearly distinguishable one dimensional Gaussian probability distributions; otherwise, most of the algorithms for threshold assessment may not be reliable. Due to the simplicity of the algorithm its fast computation is an advantage. In cases when the contrast between water and land is large enough, this method is also highly reliable. Complementary information such as a terrain model might be used to improve the results and avoid a misclassification in hilly areas.

An example of the object-based method is the image statistics-based active contour models (the so-called "snake"). This approach starts as a vector at the river centreline and grows outward to the contrasting boundaries representing the water/land boundary (Schumann et al., 2009). Other object-based methods use texture measures. These use a moving window to compute statistical properties of each pixel and its surroundings. As such, the methods classify each pixel into predefined class. The drawback of these methods is the need of training area.

## 3.2 Theoretical background and limitations

As already mentioned, the amount of backscattered signal depends on the signal and the target properties as well as on the observation geometry. All SAR sensors are side-looking instruments. Therefore, the amount of the reflected radiation is strongly dependent on the surface roughness. In case of a perfectly smooth surface, the entire signal would be reflected away from the sensor due to the so-called specular reflection. In case of a rough surface, the surface reflects the incident signal at many different angles, causing, in ideal case, diffuse reflection. These two principles are illustrated in Figure 3.1. In case of more complex surface (vegetation, buildings), also volume scattering or the so-called double bounce effect can be observed. The double bounce effect is caused by targets that form a corner reflector and thus cause that most of the signal is reflected back to the sensor.

The SAR-based water surface mapping exploits the fact that water surface is generally much smoother when compared to other land surfaces such as bare soil or vegetated land. Thus, water can often be easily detected due to its low backscatter values. However, weather conditions such as wind or rain hamper the water surface detection. As a response to wind stress or current variations short waves on the order of centimeters to decimeters are formed at the water surface, causing the Bragg resonance effect.

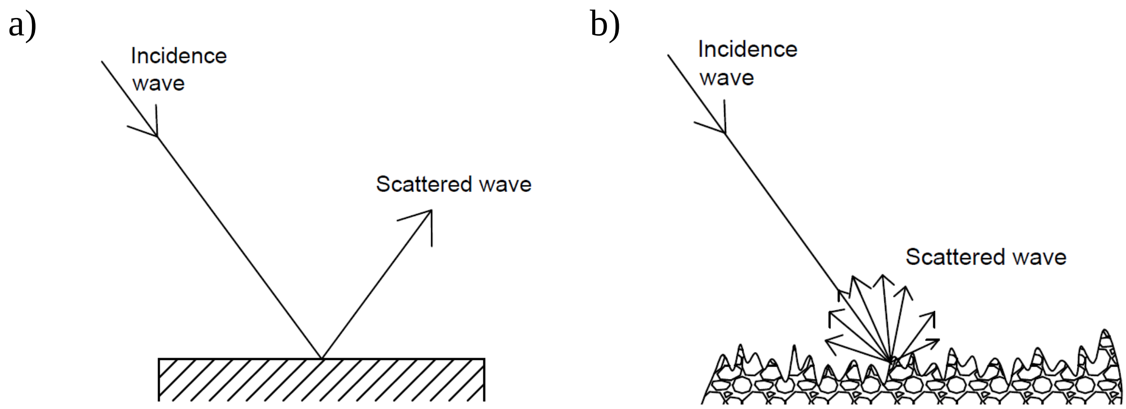


Figure 3- 1: a) signal reflection from the smooth surface, b) signal reflection from a rough surface.

The Bragg resonance effect is an enhanced backscatter signal that occurs due to a constructive interference that reinforces the backscattered signal (Figure 3.2). In particular, when the additional range distance from the radar to the successive wave crests (scaterrers) equals half of the radar wavelength or integer multiple of this value, a constructive interference will reinforce the backscattered signal from each scatterer. Clearly, the backscatter sensitivity to these short waves varies with the wavelength of the radar and the resulting backscatter intensity depends on both the wind speed and the wind direction. In case of Envisat ASAR operating on a C-Band frequency, the minimum threshold for the wind speed that can still cause the Bragg resonance effects is estimated to be at approximately 3.3 m/s at 10 m height (ESA, Radar course II; Bragg scattering). Furthermore, whereas the wave crests oriented parallel to the instrument look direction have a maximal effect on the backscatter intensity, those oriented perpendicular to the look direction might have no significant influence. Lastly, also polarisation of the incoming wave has an influence on the sensitivity to the Bragg scattering. Generally, cross polarized (i.e. HV polarisation meaning that the transmitted wave is horizontally polarized whereas the received wave vertically polarized) signal is less sensitive to the wind ripples on the water surface than the co-polarized (HH and VV) signal. In case of the co-polarised backscatter, the HH polarisation is less affected by the wind ripples than the VV polarisation (Liebe et al., 2009). Also larger waves effect the radar response from the water surface and contribute to the observed backscatter through specular reflection, breaking and modifying of the Bragg scattering waves (Hansen, 2011).

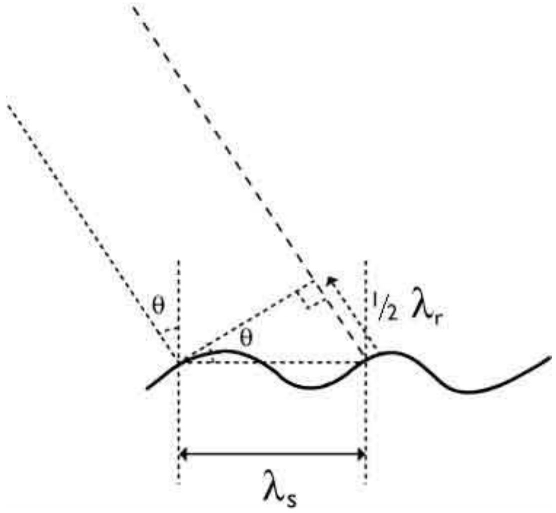


Figure 3- 2: Brag resonance effect (source: ESA, Radar course II on Bragg scattering)

As explained above, the backscatter scattered from the water surface is strongly related to the wind conditions and water currents. While this is successfully used in the oceanographic applications of microwave data, it is one the most important limiting factors for the water bodies and flood mapping over land. The majority of methods used for water surface detection (see Chapter 3.1) are based on the assumption of significantly lower backscatter intensity over water areas when compared to the land surface. The Bragg resonance effect however hampers this assumption. The effect of the wind on the water surface is illustrated already in Chapter 1 in Figure 1-1. To quantify this effect, the analysis of the influence of the wind speed on the radar backscatter and an ability of the histogram thresholding method to provide reliable results was performed over Balaton Lake using normalized NRCS ASAR WS acquisitions. The results of the analysis were used to select the acquisitions for the processing of the radial surface velocity datasets and they are presented in the Chapter 6.1.

The water surface detection using SAR acquisitions is also limited when vegetation is present in the water (e.g. during flooding in forested areas), double bounce effect can be observed, causing high backscatter values over the flooded vegetated areas. The vegetation (i.e. a tree trunk) surrounded by the water surface forms an ideal corner reflector causing double specular reflection and returning most of the signal back to the sensor. This effect is observed also in urban areas.

Moreover, in some areas, the usability may be further limited by other natural or man-made surfaces, that exhibit very similar signal reflectance as the water surface. These might be, for example, sandy dunes or other surface structures in arid and semi-arid areas, airports, or in case of very high spatial resolution, also roads. Also radar shadows caused by the high variability of the terrain might be wrongly classified as water pixels. Change detection approach or a complementary digital surface model can reduce the over-classification due to these effects (Giustarini et al., 2013).

# Chapter 4

## Radial surface velocity

### 4.1 Introduction to the radar wind observations

The wind induced resonant Bragg scattering was introduced in 3.2 and is an essential feature in the radar oceanography. Observations from active microwave sensors are successfully used to monitor wind speed and direction over the oceans as well as ocean currents (Atlas et al., 2011, Chelton et al., 2004, Verhoef et al., 2012). The prime instruments used to retrieve near-surface winds over ocean were the space-borne scatterometers. Nowadays, wind vectors are available as operational products with a spatial resolution on the order of 10 km.

For both scatterometers and SARs, the NRCS values over smooth water surfaces remain low (see 3.2) and increase as the wind increases and induces small scale ripples. The resulting backscatter intensity is dependent on both wind speed and direction relative to the instrument look angle. Various empirical geophysical mapping functions (GMF) relate the latter two parameters to the observed NRCS value with respect to the radar configuration (i.e. incidence angle, polarization and wavelength of the signal). As an example, Figure 4-1 shows the GMF for the Japanese Advanced Land Observation Satellite (ALOS) Phased Array type L-Band Synthetic Aperture Radar (PALSAR) wind product using microwave measurements in HH polarisation and with the central frequency of 1.270 GHz.

As evident in Figure 4-1, the dependency between the wind vector and measured backscatter value is ambiguous. In particular, multiple combinations of wind speed and wind direction values correspond to a single NRCS value. In scatterometry, this ambiguity is solved by combining measurements of the same area acquired from several look angles. This is possible due to the scatterometers’ ability to observe the surface using multiple beams. For example a scatterometer onboard ERS satellite used 3 beams - one perpendicular to the flight direction and two, fore-beam and after-beam, 45° before and after the mid-beam respectively. ASCAT on-board MetOp satellite employs the same configuration on each side of the satellite orbit enhancing the spatial coverage of the sensor.

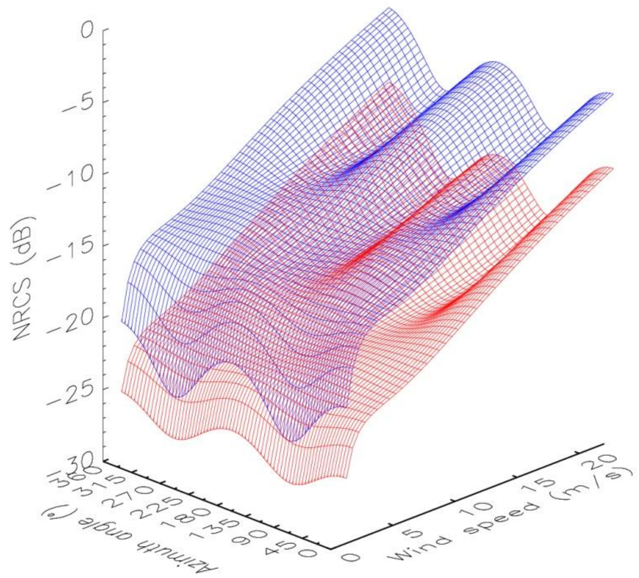


Figure 4- 1: 3D view of the L-band geophysical mapping function at 30 (blue) and 40 (red) degree incidence angles. The mapping function relates the measured Normalised Radar Cross Section of the water surface to the wind speed and direction. Source: Earth Observation Research Center.

The scatterometer measurements cannot provide reliable results over coastal areas due to the mixed land-water pixels. Given their high spatial resolution, the SAR systems offer an opportunity to map wind speed and direction over these areas. Unfortunately, the use of the SAR instruments is not as straightforward as in case of the scatterometers since as of now, there is no space-borne SAR system with a multi-beam configuration. Thus, an ambiguity in the SAR observations needs to be solved alternatively.

A variety of methods are used, typically employing some complementary information together with the measured NRCS values. Traditionally, wind direction information is supplemented from an external source such as model or temporally collocated scatterometer measurements to enable a computation of high resolution wind speed from the SAR observations. This works of course also vice versa – wind speed information is provided by model or scatterometer measurements and high resolution wind direction data are measured. Alternatively, the wind direction information may be retrieved also from the NRCS image itself with the help of visible wind streaks. The drawbacks of this approach are that the wind streaks are not always visible and also a remaining ambiguity of 180°. Generally, only one unknown parameter - usually wind speed - is the output of the traditional approach, whereas the second one - usually wind direction - is needed as an input (Dagestad et al., 2012).

Over the last decade, also two other resources have been proved useful for the SAR wind retrieval: the cross-polarized NRCS and the Doppler centroid anomaly. It was shown, that the cross-polarized SAR backscatter intensity has no dependence on the incidence angle and wind direction and is therefore proportional only to the wind speed and, in combination with the co-polarized wind data, enables the direct retrieval of the wind vectors from the SAR data. The drawback of the cross-polarized data is its higher noise floor in comparison to co-polarized dataset. This means, that the wind speed needs to be higher to get useful signal from the cross-polarized than from the co-polarized data (Vachon et al., 2011).

The Doppler centroid anomaly that can be derived from the SAR data itself was found to provide the information on the relative movement of the Earth surface towards or from the sensor in the radial (line of sight) direction. Over the oceans, the anomaly represents a mixture of sea-state displacements caused by wind, waves and currents that may be used for the wind retrieval (Mouche et al., 2012) or, under consideration of the wind influence, for the ocean currents monitoring (Rouault et al., 2010).

## 4.2 Doppler centroid anomaly and range Doppler velocity

The Doppler centroid anomaly is computed as the difference between the so-called ‘modelled’ and ‘measured’ Doppler centroid. As already explained in the chapter 2.2, the Doppler centroid corresponds to the Doppler shift of a target positioned in the antenna beam centre. The Doppler shift in frequency is proportional to the relative velocity between the source and the receiver. In case of a satellite-Earth configuration, where the satellite represents both the transmitter, as well as the receiver of the backscattered signal, the Doppler shift in the antenna beam centre is equal to:

$$f_{Dm} = 2\frac{V_{rel}}{\lambda} \tag{4.1}$$

where:

$f_{Dm}$ ... modelled Doppler shift of the signal

$V_{rel}$ ... relative velocity between the instrument and the observed Earth surface

The extra factor of 2 in equation 4.1 when compared to the equation 2.2 is necessary since the Doppler shift applies on the signal twice: The transmitted wave is Doppler shifted relative to the moving target (Earth surface) and the reflected echo is shifted in frequency again relative to the moving instrument. For vector geometry, the relative velocity between the instrument and the observed Earth surface is described as:

$$V_{rel} = \frac{\dot{r} \cdot r}{R} \tag{4.2}$$

where:

$r$ ... range vector

$\dot{r}$ ... time derivative of the range vector (range rate)

R ... range distance ( |r| )

As described for example by Raney (1986), there are two sources of motion: the spacecraft orbital velocity and Earth rotation. Range vector and range rate may thus be expressed with the help of the spacecraft vector $H$ and the scatterer location vector $R_e$:

$$r = H - R_e \tag{4.3}$$

and

$$\dot{r} = \dot{H} - \dot{R}_e \tag{4.4}$$

The equation 4.1 may thus be expressed as:

$$f_{Dm} = \frac{2}{\lambda}\left(\frac{\dot{H} \cdot R_e}{R} + \frac{\dot{R}_e \cdot H}{R}\right) \tag{4.5}$$

and, using the dot product, simplified to:

$$f_{Dm} = \frac{2}{\lambda}\left(\frac{V_{sc} R_e}{R} cos\varepsilon_2 + \frac{\omega_e \cdot H R_e cosl}{R} cos\varepsilon_1\right) \tag{4.6}$$

where:

$V_{SC}$ ... the magnitude of spacecraft orbital velocity

$\omega_e$ ... Earth rotation rate

$l$ ... latitude

$\varepsilon_1$ ... angle between the spacecraft location vector and scatterer motion vector

$\varepsilon_2$ ... angle between the spacecraft motion vector and scatterer location vector

The equation 4.6 confirms that the Doppler shift is caused both by the instrument (represented by the orbital speed of the satellite) as well as the Earth surface motion (represented by the Earth rotation rate) and is dependent on the relative position of the scatterer to spacecraft (Raney, 1986). To find the solution for a specific satellite, a specific coordinate system needs to be applied to describe the spacecraft and scatterer relative positions.

The satellite position is defined with the help of the inclination of the orbital plane (the angle between the orbital and the equatorial plane), and an argument of latitude. The argument of latitude is a parameter specifying the position of the spacecraft within the orbital plane. It corresponds to the angle between the ascending node and the current spacecraft position on the orbital plane measured from the centre of the Earth (Figure 4-2). The Earth centre, satellite sensor and the scatterer form the so-called range elevation plane. Within this plane, the range is defined as a distance between the sensor and the scatterer and the elevation angle as an angle between the spacecraft location vector and radar line of sight (Figure 4-3). The angle between orbital plane and range elevation plain is called yaw or azimuth angle. In case of side looking radars, the yaw angle is usually close to 90°. To indicate, whether the instrument looks left or right relative to the orbital velocity vector, an indicator is used with a value of +1 in case of the right looking instrument and -1 otherwise.

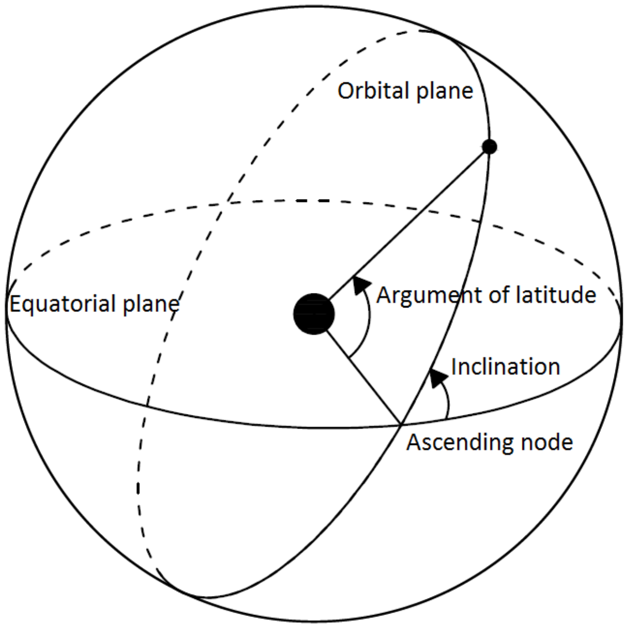


Figure 4- 2: Definition of the satellite position with the help of inclination and argument of latitude.

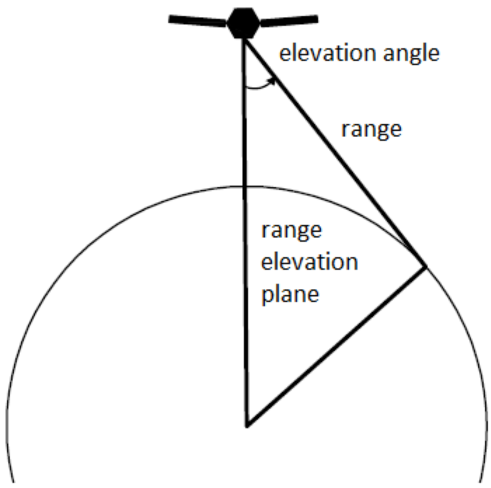


Figure 4- 3: Definition of the observation geometry within the range elevation plane.

After employing this coordinate system and the trigonometric relations between the parameters, the equation 4.6 may be expressed as (Raney, 1986):

$$f_{Dm} = \frac{k_e V_{sc}}{\pi} \sin\gamma \cos\alpha \left[1 - \left(\frac{\omega_e}{\omega}\right)(\varepsilon \cos\beta\, sin\varphi tan\alpha + cos\varphi)\right] \tag{4.7}$$

where:

| | | |
|---|---|---|
| $\omega$ | ... | angular rate of the spacecraft ($\omega_e/\omega$ equal to 14.31554 in case of Envisat ASAR) |
| $k_e$ | ... | electromagnetic wave number dependent on the signal wavelength (equal to 112 $m^{-1}$ for a radar wavelength of 5.6 cm) |
| $\varphi$ | ... | inclination of the orbit (equal to 98.55° in case of Envisat ASAR) |
| $\beta$ | ... | argument of latitude |
| $\alpha$ | ... | yaw angle of the radar beam |
| $\gamma$ | ... | elevation angle of the radar beam |
| $\varepsilon$ | ... | an indicator of the right or left looking instrument (equal to +1 in case of the Envisat ASAR) |

In the equation 4.7, the first term describes the Doppler shift arising from the spacecraft motion whereas the remaining two represent the Earth rotation contribution.

The instrument footprint geolocation parameters, elevation angle of the radar beam and thus also the modelled Doppler centroid may be calculated with the help of the Envisat CFI mission analysis software from ESA. The timing information and state vectors of the satellite are available in the ASAR WS mode product itself (Hansen et al., 2011).

Alternatively, the Doppler centroid is computed also with the help of the recorded complex echo data corresponding to the so-called measured Doppler centroid value. The absolute Doppler centroid frequency is composed of two parts - the fine Doppler frequency and an integer multiple of the azimuth sampling rate. In other words, the Doppler frequency composes of the fine part, that is ambiguous within the azimuth sampling rate. Traditionally, these two components of Doppler centroid frequency are estimated independently. In case of Envisat ASAR WS mode data, the fine Doppler frequency is estimated with the help of Madsen's method (Madsen, 1989) and further refined using the Look Power Balancing algorithm (Jin, 1996). The Doppler ambiguity is resolved by the pulse repetition frequency diversity method. The explanation of these methods is thorough and is beyond the scope of this thesis. Due to the variation of the Doppler centroid value in range, it is estimated at different ranges and a polynomial function of range is fit to the data. The value can also be updated in the azimuth direction (Envisat ASAR Product Handbook, 2007)

Since 2007, a grid of Doppler centroid frequency values is included as ancillary information in Envisat ASAR WS mode product. Each image sub-swath is divided into 20 pixels with a regular sampling within each sub-swath - corresponding to the spatial resolution of approximately 9 km in near range and 3.5 km in far range. In the azimuth direction, the spatial resolution is fixed to approximately 8 km (Hansen et al., 2011).

The Doppler centroid anomaly is computed by subtracting the modelled Doppler centroid frequency as computed in Eq. 4.7 from measured Doppler centroid from the WS mode data. The difference between these two arises from geophysical Doppler shift as well as from estimation errors of both measured as well as modelled Doppler centroid frequency:

$$f_{Dca} = f_g - f_{err} \tag{4.8}$$

where:

| | | |
|---|---|---|
| $f_{Dca}$ | ... | Doppler centroid anomaly |
| $f_g$ | ... | geophysical Doppler shift |
| $f_{err}$ | ... | Doppler centroid estimation errors |

For any surface at rest with respect to the rotating Earth, the geophysical Doppler shift is expected to be equal to zero. Therefore, over the land surface, the Doppler shift anomaly reflects only the estimation errors. On the other hand, over a dynamic water surface, the geophysical Doppler shift is related to the spatial mean of the line-of-sight velocities of the surface scattering elements weighted by their NRCS (Hansen et al., 2011, Chapron et al., 2005). This mean line-of-sight surface velocity is defined as the range Doppler velocity ($V_D$) and can be computed from the geophysical Doppler shift as:

$$V_D = -\frac{f_g * \pi}{k_e} \tag{4.9}$$

Using the local incidence angle ($\theta$), the range Doppler velocity can then be projected to horizontal plane. The radial surface velocity ($V_r$) is therefore computed as:

$$V_r = \frac{V_D}{cos\,(90° - \theta)} \tag{4.10}$$

## 4.3 Estimation errors of Doppler centroid anomaly

The quality of the Doppler centroid anomaly is dependent both on the measured as well as on the modelled Doppler centroid uncertainties. Hansen et al. (2011) identified the main sources of estimation errors in Doppler centroid anomaly as:

- measured Doppler shift error due to the NRCS gradients within the Doppler centroid estimation area ($f_{\sigma 0}$)
- predicted Doppler shift error caused by the use of wrong radar beam pointing angles ($f_{pe}$)
- residual error ($f_{\Delta}$)

and the estimation error in the Doppler centroid anomaly can be thus expressed as:

$$f_{err} = f_{\sigma_0} + f_{pe} + f_{\Delta} \tag{4.11}$$

The estimation errors are clearly visible especially over land, where the geophysical Doppler shift is expected to be equal to zero and the resulting Doppler centroid anomaly corresponds to the estimation error. Hansen et al. (2011) introduced corrections of these errors and estimated the precision of the resulting radial surface velocity. These corrections are summarized in the following chapters.

### 4.3.1 Errors in measured Doppler centroid

The accuracy of the Doppler centroid estimation from the recorded SAR return is reduced in case of large variations of the radar backscatter within the real footprint of the SAR antenna (Li et al., 1985). This occurs typically at the land-water boundaries or when corner reflectors cause double bounce effects in part of the footprint (i.e. urban areas). The presence of bright targets on one side of the Doppler centroid estimation area and weak targets on the other side results in the shift of the estimated Doppler centroid value. Simulations performed for Envisat satellite suggest, that a relative increase in backscatter by a factor 4 can cause a bias of 100Hz (Chapron et al., 2005). Hansen et al., 2011 found the relationship between the gradients of the backscatter within the Doppler centroid pixel and the Doppler centroid anomaly gradients along azimuth in neighbour hooding pixels to be linear. The parameter $c$ of this linear relationship (Equation 4.12) vary with time, polarisation and incidence angle and thus needs to be estimated using the temporally collocated scenes.

$$f_{\sigma_0} = c\Delta\sigma_{0,y} \tag{4.12}$$

where:

$\Delta\sigma_{0,y}$ ... NRCS gradient within a Doppler pixel

The correction for the measured Doppler shift error then follows (Hansen et al., 2011):

$$f_{Dca}^{\sigma_0} = f_{Dca} - f_{\sigma_0} \tag{4.13}$$

where:

$f_{Dca}^{\sigma_0}$ ... Doppler centroid anomaly corrected for bias caused by the gradients in NRCS.

### 4.3.2 Errors in predicted Doppler centroid

Errors in the predicted Doppler shift value are caused by the use of the wrong radar beam pointing angle for the computation. This departure between real and theoretical radar beam pointing angle is caused by electronic misspointing of the antenna as well as inaccurate satellite orbit and attitude parameters. For instance, an inaccuracy of the antenna yaw angle of 0.01° causes the offset of 14Hz for an elevation angle of 20° and 27 Hz for an elevation angle of 40° (Nilsson and Tildesley, 1995). There are two main effects of these inaccuracies:

- Offset of the mean Doppler centroid anomaly value from the expected zero Doppler shift over land and
- the so-called range bias.

The later will result in strong variation of the Doppler centroid anomaly values in the range direction. It is caused by the fact, that the antenna pattern is not constant along the radar beam and is therefore dependent on the elevation angle. Thus, also the bias between measured and predicted Doppler shift is a function of elevation angle. Moreover, this relationship changes in time (Hansen et al., 2011).

According to Hansen et al., 2011, both of these effects can be corrected with the help of reference data for which the geophysical Doppler shift is assumed to be equal to 0. In case of sufficient land coverage of the swath, the use of the land data from each swath is recommended. Due to a relationship between elevation angle and altitude, use of a height threshold is recommended for selection of the reference data. The predicted Doppler centroid error can then be estimated as an average of this reference data along azimuth direction and thus with the constant range and elevation angle. To obtain the geophysical Doppler shift, the estimate of predicted Doppler centroid error is subtracted from the pixels with corresponding range indices (Hansen et al., 2011):

$$f_g = f_{Dca}^{\sigma_0} - f_{pe} - f_{\Delta} \tag{4.14}$$

where:

$f_{pe}$ ... Predicted Doppler centroid error estimate for each range indices

$f_{\Delta}$ ... Residual error

## 4.4 Applicability and limitations for the water bodies detection

Mouche et al. (2012) showed that the Doppler centroid anomaly data improves the SAR sea surface wind retrieval. They derived an empirical geophysical model function describing the relationship between the Doppler shift anomalies, wind speed and wind direction with respect to the radar look direction and incidence angle for both HH and VV polarised ASAR WS data. They concluded that the Doppler centroid anomaly information is useful especially in cases of complex and rapidly changing meteorological situations, where the high resolution SAR measurements would otherwise be collocated with incorrect a priori wind direction information. However the precision requirements for this application are not yet achieved (Mouche et al., 2012).

Promising results over ocean (Wang et al., 2014, Johannessen et al., 2014) support the hypothesis that, under the severe wind conditions, the Doppler centroid anomaly dataset could be applicable also for the water surface detection over land. However, according to Li et al. (1985), the Doppler centroid estimation errors associated with the urban areas are greater than those over ocean. The correction of the Doppler centroid variations due to the backscatter gradients within the estimation pixels described in Chapter 4.3.1 reduces this effect significantly, however, the pixels with very strong backscatter variations still remain problematic and are recommended to be masked (Hansen et al., 2011). Even after the applied correction, the observed accuracy of the Doppler centroid anomaly dataset is approximately 50% higher over Amazon rain forest, where no large variations in backscatter are expected, than over all areas (Hansen et al., 2011). Errors are therefore expected at the land/water boundaries, which can be problematic especially for smaller water bodies or near urban areas where the corner reflectors occur.

Also mountainous areas can be very challenging, partly due to the high variance of backscatter values in these areas, but also due to the relationship between the Doppler centroid anomaly and elevation angle of the radar beam (see Chapter 4.3.2). Since the elevation angle is also dependent on the altitude, the correction of the errors in the predicted Doppler centroid might not be accurate enough in areas with higher altitudes.

Hansen et al. (2011) evaluated the accuracy of the Doppler centroid anomaly estimation over land below 200m altitude. The root mean square error (RMSE) of the Doppler centroid anomaly of 3.9 Hz and 4.7 Hz were achieved in HH and VV polarisation images respectively. This corresponds to the radial surface velocity of 23 and 19cm/s at 35° incidence angle. Due to the projection to the horizontal plane, the RMSE values are also dependent on the incidence angle - therefore to achieve RMSE below 30cm/s, usage of only incidence angle higher than 26° were recommended. For a lower incidence angles, the RMSE reaches up to 50cm/s.

The presented evaluation had, however, strict limitations. The land data were used as a reference to correct for the errors in the predicted Doppler centroid data. For this reason, the pixels where outliers were expected to occur were removed prior to the evaluation. This included, as already mentioned above, the areas with altitude above 200m as well as mixed land/ocean pixels or pixels with very high NRCS gradients within the Doppler centroid estimation area and the pixels with the NRCS values below -20dB (Hansen et al., 2011). Furthermore, the outliers above three times the standard deviation of Doppler centroid anomaly value over land were removed as well. In case of the inland water mapping, some of these steps cannot be performed, as they would probably mask out the areas of interest. For the purpose of this thesis, the evaluation of the precision of the data over land is therefore needed without these restrictions.

Generally, the precision of the retrieved anomaly might be a limiting factor for the water surface detection over the land together with a coarse spatial resolution of several kilometres. In combination with relatively lower wind speed over land when compared to ocean areas, the precision requirements for this application might be too high for a current ASAR WS dataset and the anomaly actually caused by the geophysical Doppler shift of the water might not be distinguishable from the retrieval errors in other areas. To evaluate the applicability of the Doppler centroid data for the inland water detection, 18 range Doppler velocity datasets derived from ASAR WS over central Europe were analysed in the following chapters. The analysis of the radial surface velocity data over inland water bodies is presented in Chapter 6.2 and the precision evaluation of the data over land pixels together with the identification of problematic land areas is presented in Chapter 6.3.

# Chapter 5

## Used data and Methodology

### 5.1 Region of interest

The ASAR WS data were processed over central Europe, with the main focus on the Lake Balaton in Hungary. 75 ASAR WS acquisitions were processed over the Balaton Lake area and thereof, 18 acquisitions were selected also for the Doppler centroid anomaly processing. The analysis of the Doppler centroid anomaly values was performed over all lakes covered by at least 5 Doppler centroid anomaly images and with the area of at least 300 $km^2$. The coverage of the Doppler centroid anomaly data is shown in Figure 5.1 and the selected lakes are listed in Table 5.1 together with the information about their Doppler centroid anomaly data coverage. The influence of the wind on NRCS values was studied only over the Lake Balaton.

| Lake name | Location | Average area [$km^2$] | Temporal coverage (Doppler centroid anomaly) |
|---|---|---|---|
| **Vänern** | Sweden | 5655 | 7 |
| **Vättern** | Sweden | 1893 | 8 |
| **Mälaren** | Sweden | 1140 | 7 |
| **Balaton** | Hungary | 592 | 18 |
| **Hjälmaren** | Sweden | 485 | 8 |
| **Neusiedl** | Austria | 315 | 16 |

Table 5-1: Lakes selected for the analysis

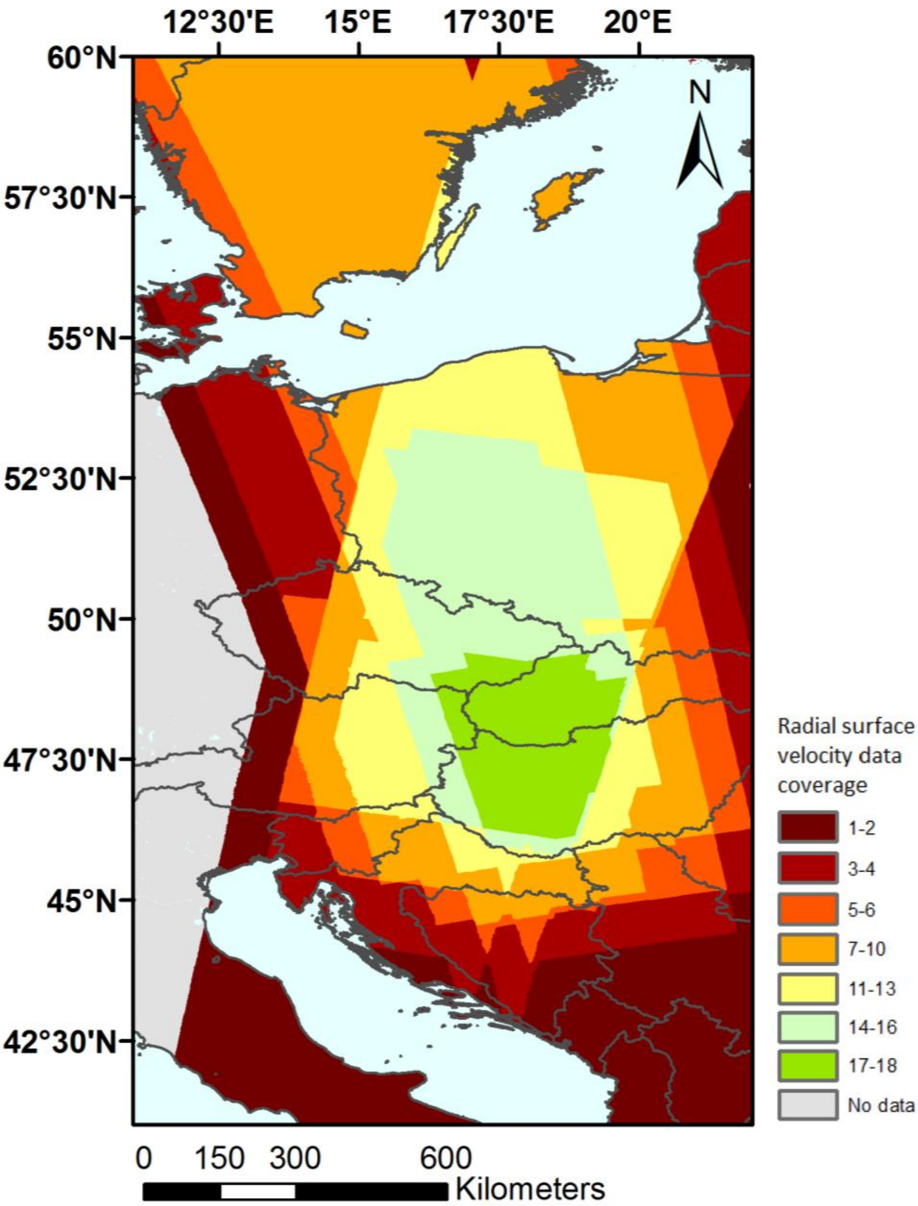


Figure 5- 1: Coverage of the selected radial surface velocity datasets

## 5.2 Used datasets

### 5.2.1 ASAR WS NRCS and Doppler centroid anomaly data

The ASAR WS data described in detail in Chapter 2.3 were used in this work. For the analysis of the wind influence on the backscatter measurements, ASAR WS acquisitions were processed over the Lake Balaton covering the time span of May 2005 to May 2011. The data acquired during the winter time (15th November to 1st April) were not used as these may have been affected by the frost on the water surface. Overall, 75 ASAR WS acquisitions were processed and analysed

The Level 1b ASAR WS data were geocoded using the Next ESA SAR Toolbox (NEST) software, version 4A. The geocoding of a SAR image consists of applying a geometric transformation from the initial 2D radar geometry (range and azimuth distance) to the map projection with an associated datum. The geocoding procedure in NEST software included the following steps:

- The Doppler Orbitography and Radiopositioning Integrated by Satellite (DORIS) precise orbit files were applied to determine the exact platform position in space.
- The Range-Doppler terrain correction using the Shuttle Radar Topography Mission (SRTM) digital elevation model (DEM) was performed. In this step, the image pixels were projected onto the reference DEM with the help of the exact platform position and range and azimuth distance. This method requires no tie points selection.
- A radiometric normalization was applied and the computed σ0 values were converted to decibels.

In general, the radar backscatter is strongly dependent on the local incidence angle. This effect is even more pronounced over water than over land surface. To allow for the comparison of the data acquired from different satellite orbits, and thus with different viewing geometry, the data were normalized with respect to the local incidence angle. For each data pixel location, a linear model was fitted to the backscatter measurements as a function of the local incidence angle and the measurements were adjusted to the local incidence angle of 30° following the equation 5.1 (Sabel et al., 2012):

$$\sigma^0(30,t) = \sigma^0(\theta,t) - \beta(\theta - 30) \tag{5.1}$$

where:

$\sigma^0(30,t)$ ... normalized NRCS (sigma0) value at the acquisition time $t$

$\sigma^0(\theta,t)$ ... original NRSC (sigma0) value at the acquisition time $t$ and with local incidence angle $\theta$

$\beta$ ... slope parameter describing the linear relationship between backscatter and local incidence angle for each data point

As a result, a set of normalized NRCS images for Balaton Lake and its surroundings was created.

The Doppler centroid anomaly data were provided by Dr. Morten W. Hansen from Nansen Environmental and Remote Sensing Center (NERSC) in Norway using their processing software created in MATLAB. The data were provided in form of radial surface velocities projected on the horizontal surface (see equations 4.9 and 4.10). Apart from the radial surface velocities, the data include also the corresponding radar look direction information, RMSE information based on the quality assessment presented in Hansen et al. (2011) and an initial mask. The mask flags the pixels with higher radial surface velocity value than three times RMSE, areas located near the land/ocean border, areas with high NRCS gradients within the Doppler centroid estimation area and those with NRCS values below -20dB as invalid.

The processing chain is described in Hansen et al. (2011) and summarized in Chapters 4.2 and 4.3. 18 acquisitions of the Balaton Lake were selected for the analysis based on the results presented in chapter 6.1.

### 5.2.2 Wind speed and direction data

The normalized backscatters as well as the Doppler centroid data were compared with the wind speed and, in case of Doppler centroid data, also wind direction information. For this purpose, modelled wind data from the ERA-Interim reanalysis (Dee et al., 2011) and the DS512.0 global synoptic meteorological data set (source: U.S. Climate Prediction Center) from the World Meteorological Organisation (WMO) stations were used. The DS512.0 data set comprises the wind direction and wind speed in knots with a temporal step of 3 hours. The DS512.0 in-situ data were used only for the analysis of the wind influence on the NRCS measurements over Balaton and for this purpose, the station located in Siófok city (latitude: 46.92°N, longitude: 18.03°E) was selected.

The ERA-Interim reanalysis data is produced and provided by the European Centre for Medium-Range Weather Forecasts (ECMWF). It includes large number of surface as well as upper-air parameters, describing weather as well as ocean-wave and land-surface conditions. The data are provided in a grid with a spatial resolution of 0.75° and temporal resolution of 3 or 6 hours, depending on the parameter. The reanalysis data are available via the ECMWF data server and range back to 1979 . The wind data include 10-meters $u$ and $v$ wind components in m/s with a temporal resolution of 6 hours (at 0, 6, 12 and 18 o'clock). The $u$ component represents the east-west component of the wind while the $v$ component represents the north-south wind motion. These can be converted into wind speed ($v_{wind}$) and direction ($d_{wind}$) using equations 5.2 and 5.3:

$$v_{wind} = \sqrt{u^2 + v^2} \tag{5.2}$$

$$d_{wind} = 270° - atan\left(\frac{v}{u}\right) \tag{5.3}$$

For each radial surface velocity data pixel, the data from the nearest ERA-Interim grid location was selected. Temporally, the nearest wind measurement to each ASAR WS acquisition was selected resulting into the maximal temporal difference of 3 hours between the ASAR WS acquisition and modelled wind vector. The wind conditions can change substantially in time,

### 5.2.3 Reference datasets

As a reference dataset, the Corine Land Cover data was used (Bossard et al., 2000). The Corine

Land Cover employs 44 land cover classes with a minimal mapping unit of 25 ha in case of an areal phenomena and 100 m width in case of line phenomena. The inventory was initiated in 1985 and is produced by visual interpretation of the high resolution satellite imagery. It is regularly updated. In this work, version from year 2006 created using the dual date 'Satellite Pour l'Observation de la Terre' (Satellite for observation of Earth, SPOT) 4/5 and Indian Remote-Sensing Satellite (IRS) P6 Medium Resolution Linear Imaging Self-Scanner (LISS III) data was used.

The Corine Land Cover data has a spatial resolution of 100m. To simplify its application in our analysis, the Corine data were resampled using the nearest neighbour resampling to the ASAR WS grid with a pixel spacing of 75m.

## 5.3 Methodology

The analysis presented in this study can be divided in three parts. First, the influence of the wind speed on the backscatter measurements over water surfaces was analysed with the help of available modelled and in-situ measured wind data. The objective was to see, which wind level has a potential to hinder the successful land/water detection and to select acquisitions above this level for the Doppler centroid anomaly analysis. Second, similar analysis was performed for the Doppler centroid anomaly data for the selected images to assess the relationship between the radial surface velocity and the wind speed in the radar look direction. Lastly, the precision of the selected Doppler centroid anomaly datasets was assessed over land to see, whether the radial surface velocity values induced by wind may be distinguishable from noise.

### 5.3.1 Influence of wind on the NRCS measurements

The Bragg scattering effect is visible in the C-Band radar image of water surface if the wind speed exceeds 3.3m/s (ESA, Radar course II on Bragg scattering). Above this threshold, the amount of returned signal increases with the increasing wind speed and is dependent also on the wind direction relative to the radar look angle and the signal polarisation.

In the first part of this work, the mathematical relationship (expressed by the Pearson correlation coefficient *R*) between the wind speed and backscatter return from the water surface was analysed over the Balaton Lake. The water maps were generated from the normalized backscatter images using the histogram thresholding method. The resulting maps were compared to the reference data from the Corine Land Cover inventory. The results were related to the wind speed information from ERA-Interim model and WMO meteorological station measurements in Siófok city.

Due to the large number of images, the automated Otsu method (Otsu, 1975) was used to derive the histogram thresholds for the land/water surface classification. This method is commonly used for the SAR image classification. It is based on the assumption, that each image contains two classes of pixels (in this case, the water and land pixels). As an input, a grey-level histogram of the SAR image is provided and the optimum threshold is calculated so that the intra-class variance of the two classes is minimal. A binary image showing the two classes is the output of the method.

An algorithm introduced by Greifender (2012) was used for the image classification with small modifications. The image classification comprised of the following steps (Greifender, 2012):

- The image grey-level histogram was normalized and transformed to the values from 0 to 255.
- The image was divided into overlapping subsets of 100 by 100 pixels and only the subsets containing a sufficient portion of both classes (land and water) were selected using the measure of contrast within the subset introduced by Martinis et al. (2009).
- A so-called Lee Filter was applied to reduce the speckle noise in the SAR image and a Canny Edge filter was applied to mask the areas around the edges within the image. The edge areas often contain a large number of mixed pixels which can distort the threshold result, thus they were ignored for further processing (Liu & Jezek, 2004)
- An individual threshold was calculated for each of the selected subsets. This was done by an iterative calculation through all possible thresholds and searching for the minimal intra-class variance. The final threshold was computed as a mean of the sub-images thresholds.

The correspondence between the Corine Land Cover based water map and the corresponding ASAR WS water maps was quantified using a confusion matrix as presented by Provost and Kohavi (1998) and the Coen's kappa ($\kappa$) coefficient. The confusion matrix summarises information about true and predicted classifications performed by the classification system. In the context of this work, the confusion matrix entries have the following meaning (see also Table 5.2):

- $a$ is the number of correct predictions that the pixel represents the water surface.
- $b$ is the number of incorrect predictions that the pixel represents the water surface.
- $c$ is the number of incorrect predictions that the pixel represents the land surface.
- $d$ is the number of correct predictions that the pixel represents the land surface.

The *true* stands for the water map created from the Corine Land Cover data and the *predicted* for the water map created from the respective normalized ASAR WS image.

| | | **Predicted** | |
|---|---|---|---|
| | | Water | Land |
| **True** | Water | *a* | *b* |
| | Land | *c* | *d* |

Table 5-2: The schema of a confusion matrix

Using the information stored in the confusion matrix, the $\kappa$ coefficient can be computed as a single value statistical measure of the inter rater agreement. $\kappa$ is generally thought to be a more robust measure than simple percent agreement calculation as it takes into account the agreement occurring by chance. The $\kappa$ coefficient is computed as follows:

$$\kappa = \frac{Pr(a) - Pr\ (e)}{1 - Pr(e)} \tag{5.4}$$

where:

*Pr(a)* ... relative observed inter rater agreement

*Pr(e)* ... hypothetical probability of chance agreement

These measures can be computed from the confusion matrix coefficients:

$$Pr(a) = \frac{a + b}{a + b + c + d} \tag{5.5}$$

$$Pr(e) = \frac{(a + b) * (a + c) + (c + d) * (b + d)}{(a + b + c + d)^2} \tag{5.6}$$

The $\kappa$ coefficient has a value of 1 in case of a complete agreement and 0 in case, that there is no other agreement than what would be expected by chance as defined by *Pr(e)*.

### 5.3.2 Doppler centroid anomaly over ocean and inland water bodies

The analysis of the relationship between wind speed and direction and the radial surface velocity data was performed for the selected inland water bodies and, for the reference, also over the Baltic Sea. The results were presented in the form of scatter plots and the corresponding $R$ values were computed. The ASAR WS scenes selected in the previous step (Chapter 6.1) were used. The wind speed in the radar line-of-sight direction was computed with the help of the ERA-Interim modelled wind vector and the corresponding radar look direction for each radial surface velocity pixel. The wind speed product was then compared to the available radial surface velocity values.

The most obvious limitation of the ASAR WS radial surface velocity dataset for the inland water bodies detection is its low spatial resolution. Even though only lakes with an area over 300 $km^2$ were selected, the pixel area may still be too large to be covered only by water. The Figure 5.2 shows centres of Doppler centroid anomaly pixels over lakes Balaton and Neusiedl in case of the acquisition from 14th October 2009. Apparently, almost no pixel is filled exclusively with water. The same applies also for the lake Hjälmaren in Sweden (not shown). As the land/water boundary often introduces a strong gradient in the backscatter, the mixed land/water pixels or pixels located near to this boundary are expected to cause outliers in the relative surface velocity dataset. This can further increase the requirements on the water body extent. As a result, even large water bodies such as Balaton Lake may not be detectable by the radial surface velocity data derived from the ASAR WS. The analysis of the radial surface velocity values over inland water bodies are therefore separated into a) water-only and b) mixel land/water pixels. The objective was to evaluate, whether also the mixed pixels can provide any information about the wind speed.

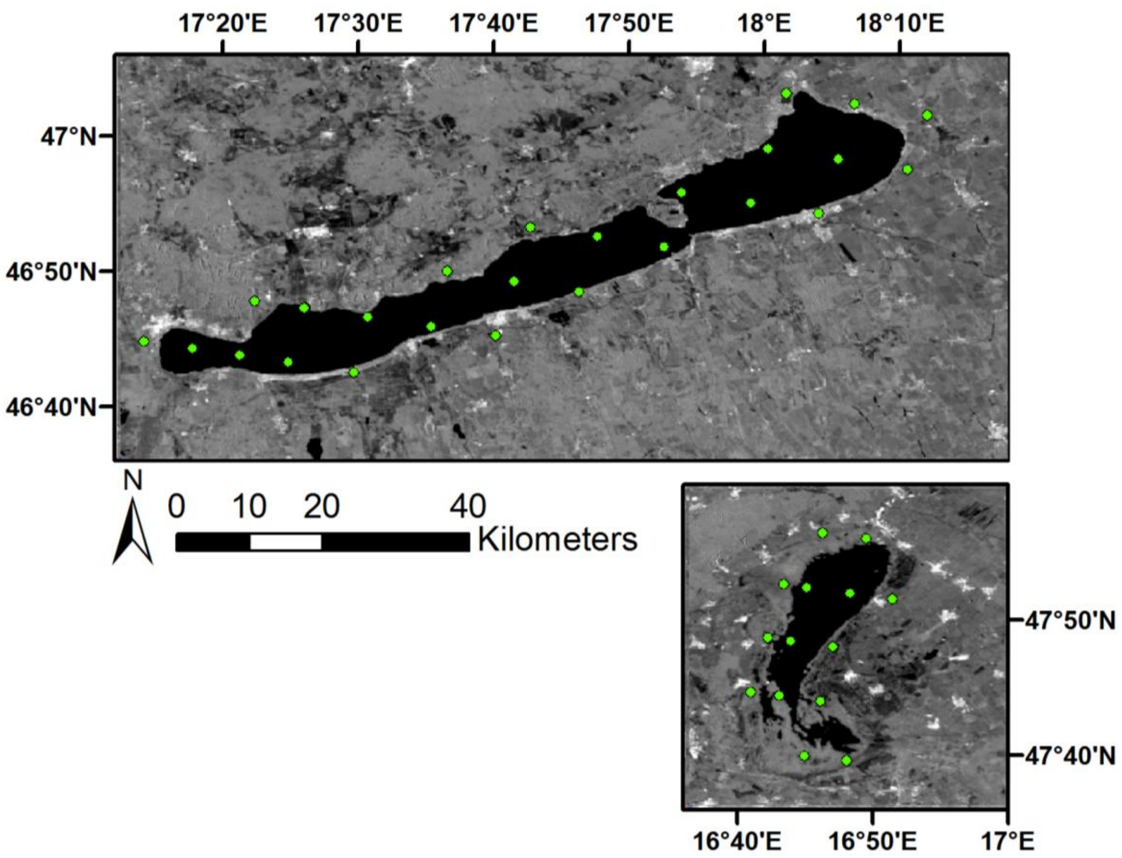


Figure 5- 2: Mean backscatter images with the location of the centres of the Doppler centroid anomaly pixels (green circles) over lakes Balaton (up) and Neusiedl (down). Black colour highlights the water areas.

### 5.3.3 Doppler centroid anomaly data over land

The expected value of the radial surface velocity over land surface is equal to zero. The derived values thus correspond directly to the retrieval errors. In other words, the RMSE values over land should provide an estimate about the accuracy of the retrieved velocities. Global precision analysis was performed by Hansen et al. (2011) using 325 images in VV polarisation and 149 images in HH polarisation distributed worldwide. However, as already explained in chapter 4.4, these results were obtained using very strict limitations on the pixel selection.

To obtain retrieval accuracy assessments for the application of the Doppler centroid anomaly over land, the RMSE analysis was performed for all available land pixels from the selected acquisitions. The water and mixed land/water pixels were excluded to ensure, that no geophysical shift will influence the results. The water and mixed water/land pixels were classified with the help of the Corine Land Cover inventory as those, where at least 10% of the Doppler centroid anomaly estimation area is classified as ocean, inland water body or river area.

Due to the projection of the range Doppler velocities (i.e. velocity measured in the radar line of sight direction) to the horizontal plane (see equation 4.10), the retrieval accuracy of the relative surface velocity is also dependent on the local incidence angle. The same retrieval error in the range Doppler velocity will thus cause twice as large error in the relative radial surface velocity in case of an incidence angle of 20° than in case of 40° (Hansen et al., 2012). To obtain comparable results for all incidence angles, the relative surface velocity values were computed back to the range Doppler velocities using the local incidence angle.

Based on the results, the areas prone to outliers in the relative surface velocity were identified. Also, the resulting RMSE values were compared to the wind induced surface velocity values over inland water bodies to assess, whether these may be distinguished from noise using a single threshold.

# Chapter 6

## Results

### 6.1 Influence of wind on the NRCS measurements

Figure 6.1 shows the relationship between wind speed and average normalized Backscatter over Balaton lake area. As expected, a relatively high correlation (*R* of 0.71 in case of ERA-Interim and 0.59 in case of WMO in-situ wind speed data) is measured. The lower *R* in case of the WMO station in Siófok may be influenced by the fact, that the WMO wind measurement only represents one location in Siófok city, whereas the ERA-Interim modelled wind vector approximates the wind speed over larger area (0.75x0.75°). The average normalized backscatter increases with the increasing wind speed and in case of very high wind speed values (>10m/s) exceeds -10dB what makes it comparable to the surrounding land surface.

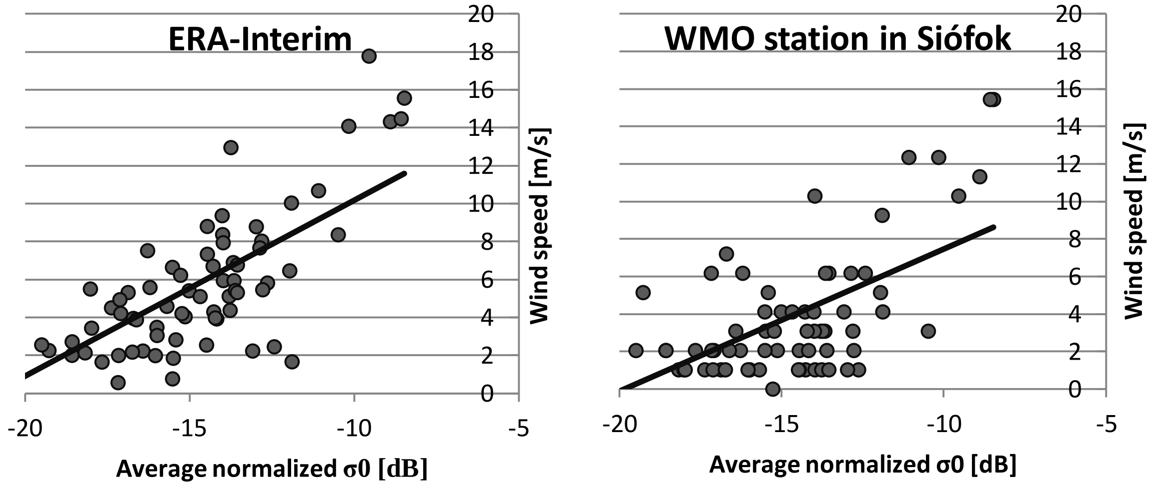


Figure 6- 1: The scatter plots of the average normalized ASAR WS σ0 values over Balaton Lake and corresponding wind speed from ERA-Interim model (left) and WMO meteorological station in-situ measurements (right).

The influence of this relationship on the reliability of the histogram thresholding method for the water surface mapping is demonstrated in the Figure 6.2. Histograms over land (black line) and water (blue line) pixels according to the Corine Land Cover classification are presented for three different ASAR WS scenes. The top histogram shows the image acquired on 2nd October 2005 with a wind speed of 1.2 m/s according to the ERA-Interim data. This value is far below the

Bragg scattering effect threshold. The land and water pixels can be separated using the threshold of -14.8 dB and the κ value equals to 0.95. The middle histogram represents the acquisition from 7th May 2008 and a wind speed of 7.5m/s. The land and water pixels distribution is partly overlapping, reducing the κ value to 0.61 due to the large number of misclassified pixels. The bottom histogram shows the same scene under a severe wind conditions with a wind speed of 14.5m/s. This image was acquired on 15th May 2010. In this case, the histogram thresholding method cannot provide any reliable results. The κ coefficient of 0.08 shows, that there is no agreement apart from that by a chance.

Generally, 50% of the derived water maps showed good correspondence with the κ coefficient over 0.8. The average wind speed of these acquisitions was equal to 4.2 m/s. On the other hand, 11% of the measurements showed κ values below 0.4 with an average wind speed of 10.6 m/s according to the ERA-Interim modelled wind speed data. The correlation coefficient between the κ value and the corresponding wind speed equals to -0.62 and -0.63 in case of the ERA-Interim modelled data and the in-situ WMO dataset respectively. This result confirms a strong influence of the wind speed on the ability of the histogram thresholding method to delineate the land and water surfaces. It needs to be noted, that also other effects influence the result. These include wind direction relative to the radar look angle, the signal polarisation or the properties of the surrounding land surface and therefore the resulting contrast between land and water surface (Liebe et al., 2009).

The scatter plot between κ value and wind speed (Figure 6-3) reveals, that most of the images acquired under severe wind conditions (the wind speed of 8m/s and higher) have κ value below 0.6. On the other hand, some acquisitions show enhanced backscatter over water surface even though the wind speed was below the Bragg scattering effect threshold. The possible explanation may be that of Liebe et al. (2009) who concluded, that minor wind gusts in the radar look direction may cause the Bragg scatter to occur even though the wind speed is very low. This is well illustrated in Figure 6-4, that shows an acquisition from 13th July 2007 with a high backscatter variability over water for wind speed conditions of 2.3 m/s according to ERA-Interim data. The areas of the enhanced backscatter are most likely caused by the localized wind gusts in the sensor look direction.

In case of some acquisitions, κ values remain high even under high wind conditions. This can be explained by the influence of wind direction that was ignored in the presented analysis. High wind speed in the direction perpendicular to the radar look direction may have no influence on the radar backscatter. For instance, κ of 0.87 was achieved in case of the acquisition from 27$^{th}$ May 2009 even though the ERA-Interim modelled wind speed was equal to 12.7 m/s over Balaton Lake. However the wind direction was almost in line with the sensor orbital direction and the influence of the wind induced ripples on the measured NRCS values was therefore minimized.

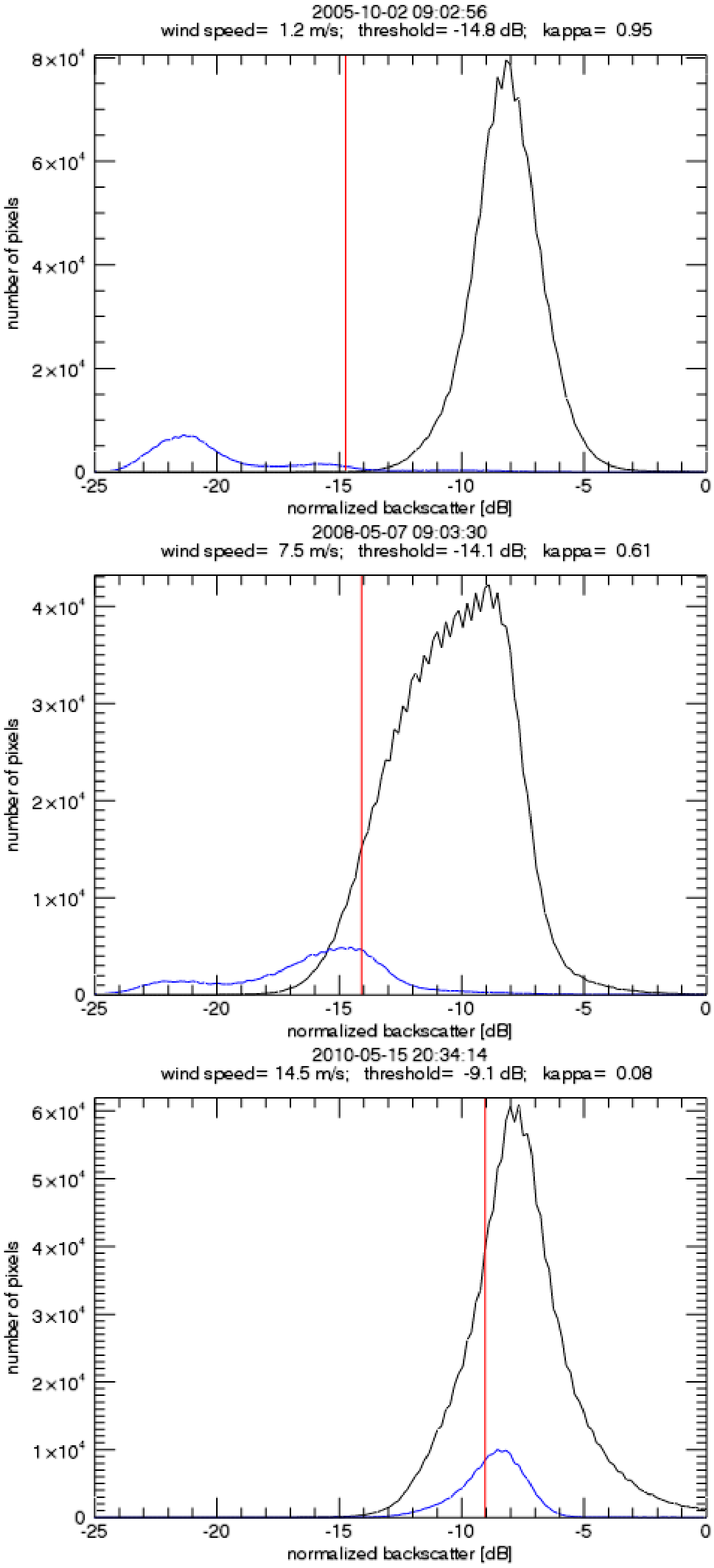


Figure 6- 2: The histograms of a radar backscatter for Light Air (top), Moderate Breeze (middle) and Near Gale (bottom) according to the Beaufort wind scale. The threshold derived by Otsu's method (Otsu, 1979) is plotted red, black colour represents land pixels and blue water pixels.

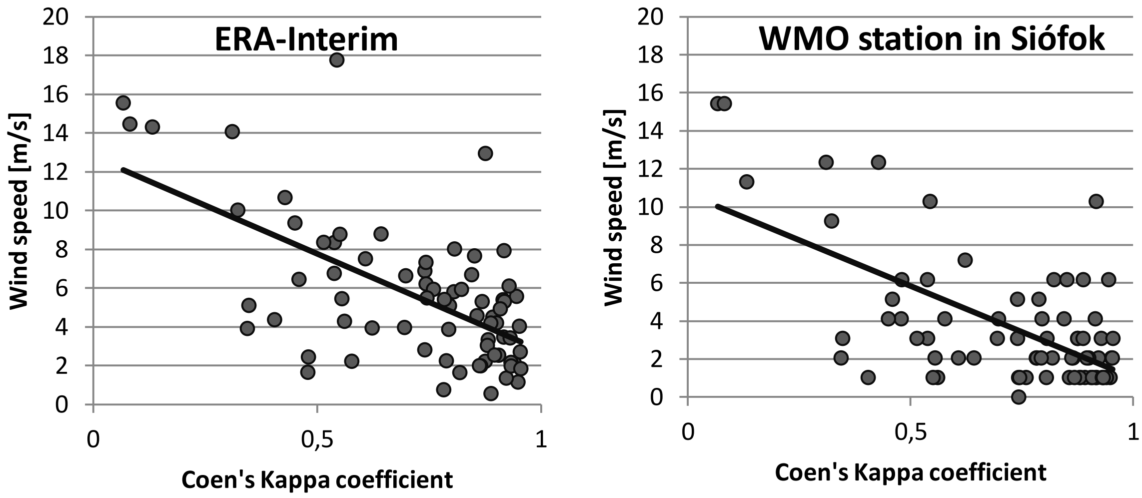


Figure 6-3: The scatter plot of κ value and wind speed according to ERA-Interim model (left) and WMO in-situ measurements (right).

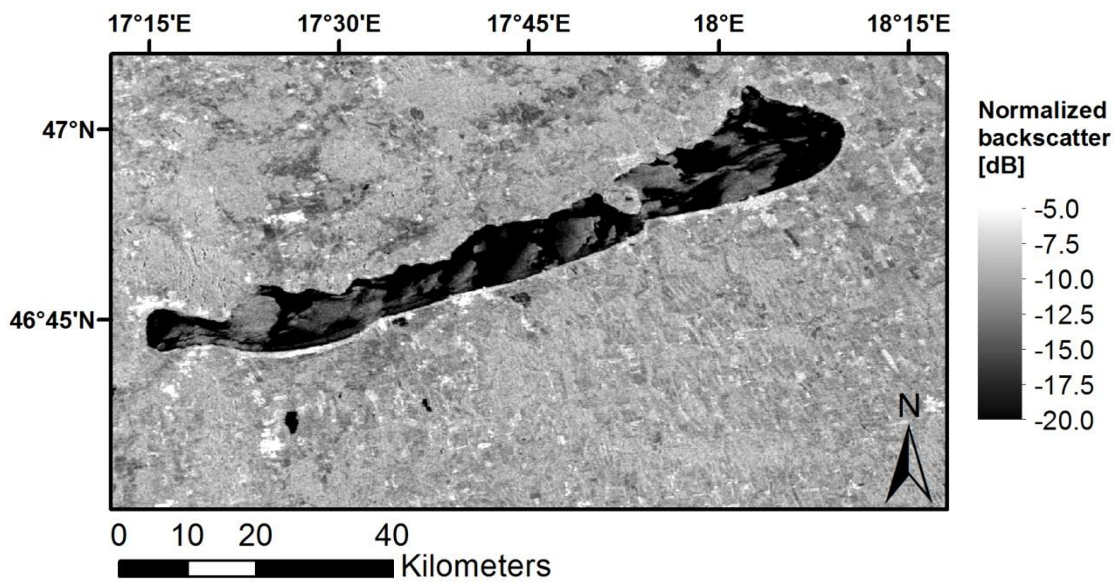


Figure 6-4: Normalized backscatter over Lake Balaton on 13th July 2007 with a wind speed of 2.3 m/s. The areas of high backscatter over the water are most likely caused by the localized wind gusts in the sensor look direction.

Based on these results, 18 ASAR WS scenes were selected for the Doppler centroid anomaly data processing. Thse are summarized in Table 6.1 together with the corresponding κ coefficients and ERA-Interim wind speeds. Due to the unavailability of the Doppler centroid data before June 2007, acquisitions from previous years could not be included in the Doppler centroid data analysis. Apart from the acquisitions with high wind speed (over 5km/h) and low κ coefficients (below 0.7), also few images acquired under calm water conditions with a corresponding high kappa value were selected as a reference data. Images covering larger swaths and therefore also the other lakes selected for the evaluation were also given priority.

| Acquisition time | Polarisation | Satellite orbit | κ | Wind speed [m/s] |
|---|---|---|---|---|
| **30th June 2007; 20:34:50** | VV | Ascending | 0.73 | 0.9 |
| **27th September 2007; 20:37:04** | VV | Ascending | 0.91 | 2.5 |
| **7th May 2008; 09:03:30** | VV | Descending | 0.61 | 7.5 |
| **23rd May 2008; 09:02:54** | VV | Descending | 0.54 | 6.8 |
| **23rd May 2008; 20:25:21** | VV | Ascending | 0.62 | 3.9 |
| **20th August 2008; 09:01:12** | VV | Descending | 0.56 | 5.5 |
| **27th May 2009; 09:01:07** | HH | Descending | 0.88 | 13.0 |
| **17th July 2009: 20:25:54** | VV | Ascending | 0.88 | 2.6 |
| **14th October 2009; 09:17:14** | VV | Descending | 0.07 | 15.6 |
| **14th October 2009; 20:26:18** | VV | Ascending | 0.13 | 14.3 |
| **17th October 2009; 20:34:15** | VV | Ascending | 0.93 | 3.4 |
| **12th May 2010; 20:28:15** | VV | Ascending | 0.70 | 4.0 |
| **15th May 2010; 20:34:14** | VV | Ascending | 0.08 | 14.5 |
| **22nd August 2010; 20:22:53** | VV | Ascending | 0.69 | 2.4 |
| **25th August 2010; 20:28:18** | VV | Ascending | 0.58 | 2.2 |
| **13th September 2010; 20:28:32** | VV | Ascending | 0.87 | 5.3 |
| **18th October 2010; 20:30:59** | VV | Ascending | 0.85 | 7.7 |
| **6th April 2011; 09:11:22** | HH | Descending | 0.45 | 9.4 |

Table 6-1: Doppler centroid anomaly data used for the analysis

## 6.2 Doppler centroid anomaly over ocean and inland water bodies

The results of the radial surface velocity analysis over water surface were divided into following classes:

- pixels located over the Baltic Sea and covered solely by water
- pixels located over the inland water bodies and covered solely by water
- mixed land/water pixels located over the inland water bodies.

The last class was further separated into four subclasses according to the water portion within the pixel.

Over 34,000 pixels from 13 ASAR WS acquisitions were used for the analysis over the Baltic Sea

(Figure 6-5). *R* of 0.85 confirms strong linear relationship (Figure 6-5 (a)). It should be noted, that the mask proposed by Hansen et al. (2011) (see Chapter 5.2.1.) was used to compute the scatter plot. Without the masking, *R* reduces to 0.50due to a large number of outliers, that are mostly located near the coastlines and in the areas of high backscatter variations.

Figure 6-5 (b) shows two ASAR WS acquisitions over the Baltic Sea region together with the temporally corresponding ERA-Interim modelled wind vectors. In the upper image, the wind direction over the Baltic Sea was predominantly in WestSouthwest direction, almost parallel with the ASAR look direction, and the wind speed reached up to 25m/s. The resulting radial surface velocity over the water surface ranges between -1 and 4 m/s and its patterns spatially correspond to those of the ERA winds – the increasing winds towards southwest are reflected by the decreasing radial surface velocities.

In the lower image, the wind direction varied between East and SouthEast direction with the wind speeds up to 10m/s in southwest. The radial surface velocities ranged between 0.5 and 1.5 m/s and also increase towards southwest where values up to 4 m/s can be observed.

A lot of outliers are apparent on the lower image in northwest. East of the Swedish coast, a lot of pixels show exceptionally high velocity values; in some cases exceeding +/-10 m/s. These are caused by a very strong variation of backscatter values in this area (not shown). Furthermore, outliers are present also at the coast of Germany and Sweden. Hansen et al. (2011) defined these problems and proposed a masking of these areas. This approach is, however, not applicable for the inland water bodies mapping. First, for masking of the pixels proximal to land, the a-priory knowledge of the land/water boundary location is required. Second, the backscatter variation over land is generally quite high, especially in the urbanized areas.

**a)**

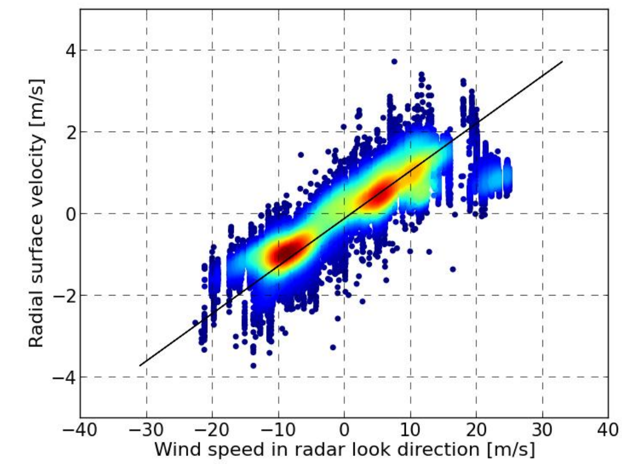


**b)**

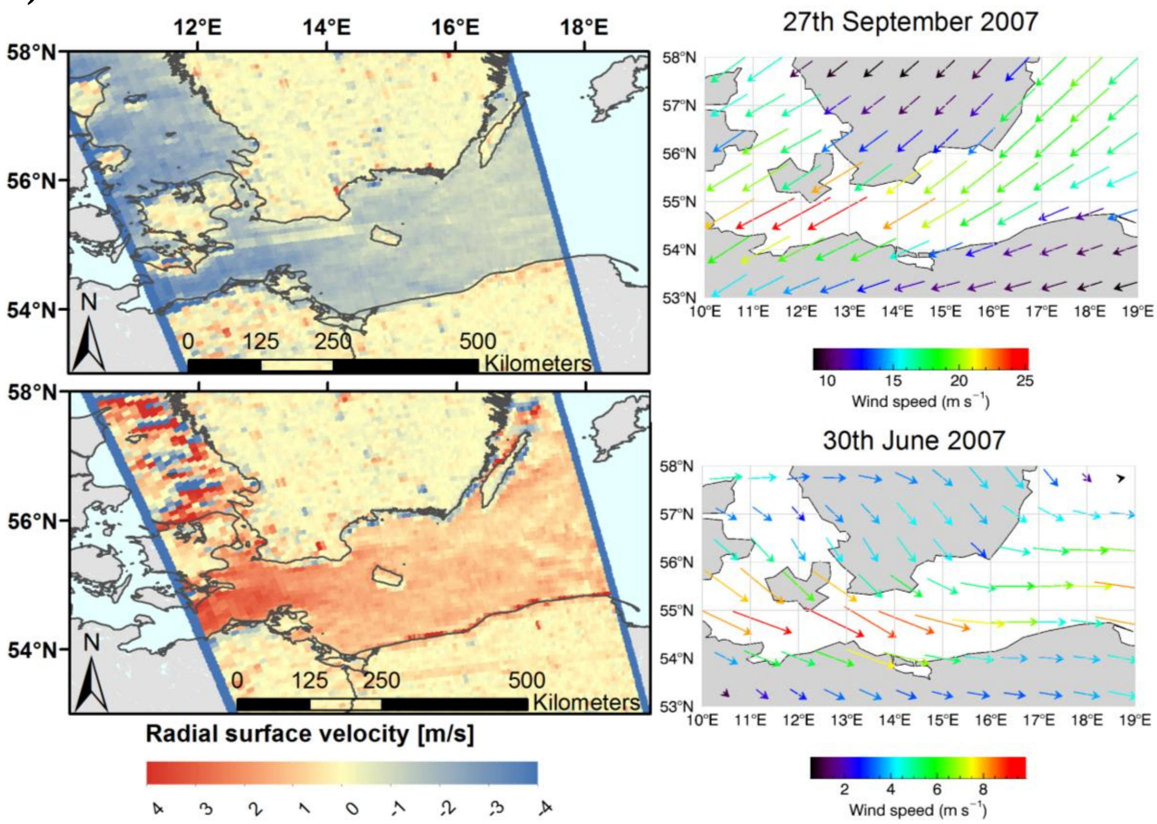


Figure 6-5: a) Scatter plot of ERA-Interim wind speed in the radar look direction and the radial surface velocity over Baltic Sea, b) Examples of radial surface velocity data over the area (left) together with the corresponding ERA-Interim wind vectors (right). Up: ASAR WS acquisition from 27th September 2007 acquired at 20:37 and the ERA-Interim wind vectors from 28th September 2007 at 0:00, down: ASAR WS acquisition from 30th June 2007 acquired at 20:34 and the ERA-Interim wind vectors from 1st July 2007 at 0:00

Figure 6-6 shows the relationship between wind speed and radial surface velocities over several lakes in Southern Sweden. Only pixels covered solely by water were selected. The images were taken at the same date as those presented in Figure 6-5 (b). The scatter plot was computed using only valid radial surface velocity values according to Hansen et al. (2011). 413 pixels from 9

ASAR WS acquisitions were used for the scatter plot. Although the wind speed and the radial surface velocity range are considerably lower than in case of the Baltic Sea, the correlation remains high (*R*=0.79). Without the masking, *R* decreases to 0.51 due to the outliers located mainly near the lake coastlines.

The examples of radial surface velocity datasets over lakes Vättern and Vänern (Figure 6-6 (b)) illustrate the problems associated with the radial surface velocity values derived over the inland water bodies. The relationship between wind speed in the radar look direction and radial surface velocity remains strong also for the inland water as long as the pixel is fully covered by water and no large backscatter variations are present within the Doppler centroid estimation area. However, for the purpose of water bodies mapping, the presented example reveals a number of limitations.

First, the spatial resolution remains the most important limiting factor in case of the Envisat ASAR radial surface velocity dataset. Only 15 pixels from the total of 18 acquisitions of the lakes Balaton and Neusiedl are covered by water only. This means that even for a lake with an area of almost 600 $km^2$, only mixed land/water pixels can be expected. This limitation will be probably eliminated with the improved spatial resolution of the Doppler centroid data of the future sensors such as Sentinel-1 (Engen et al., 2014)

Second, the wind speeds over the inland water bodies are generally considerably lower than over sea and thus the resulting Bragg scattering effect doesn't induce significantly different radial velocity values. For instance, at midnight between 27$^{th}$ and 28$^{th}$ September, the wind speed reached up to 25 m/s over the Baltic Sea, whereas over the land areas, the values ranged only between 6 and 10 m/s. These values are high enough to cause the Bragg scattering effect and enhance the backscatter from the water surface, especially when the wind direction is within 30° to the radar look direction. However, the wind induced radial surface velocity is only between 1 and 2 m/s over most of the water area. This value might not be distinguishable from the surrounding noise. Especially the acquisition from 30$^{th}$ June 2007 is quite noisy and a large number of pixels with comparable or even higher magnitudes are located over the surrounding land areas.

The acquisition from 30$^{th}$ June 2007 (Figure 6-6(b), bottom) illustrates the third limitation when deriving radial surface velocities. This is related to the outliers caused by the strong NRCS gradients within the Doppler centroid anomaly estimation area. Over the Vättern Lake (located approx. at 58°N and 15°E), the wind speed ranged only between 1 and 4m/s. and the wind direction was close to the ASAR orbiting direction. As a result, NRSC values over the lake are very low (-15 to -23 dB) when compared to those of the surrounding land (-8 and -12 dB). These conditions are ideal for NRCS based water surface mapping, but it is quite problematic in case of the Doppler centroid data. According to Hansen et al. (2011), the NRCS values below -20 dB make the interpretation of the geophysical shift highly uncertain and are therefore recommended for masking. Furthermore, high negative velocities (up to -8 m/s) on the western side of the lake as well as the comparably high positive velocities on the eastern side are presumably caused by the strong backscatter variation at the lake coast, even though the pixels are located over the water. As explained in Chapter 4.3.1, the presence of bright targets on one side of the Doppler centroid estimation area and weak targets on the other side results in the shift of the estimated Doppler centroid value. Apparently, not only the pixels located directly at the land/water boundary, but also those located nearby are affected. Similarly, outliers are located near the coast of the Lake Vänern (59°N, 13.5°E). Generally, in case of low NRCS values over water, the proximity to land and the related backscatter variation hampers the radial surface velocity retrieval over the water surface. For the application of detection of water bodies under the severe wind conditions, this limitation is not relevant as long as the backscatter values over water is comparable to those over land surface. This is often the case if the wind speed exceeds approximately 8km/h (see Chapter 6.1).

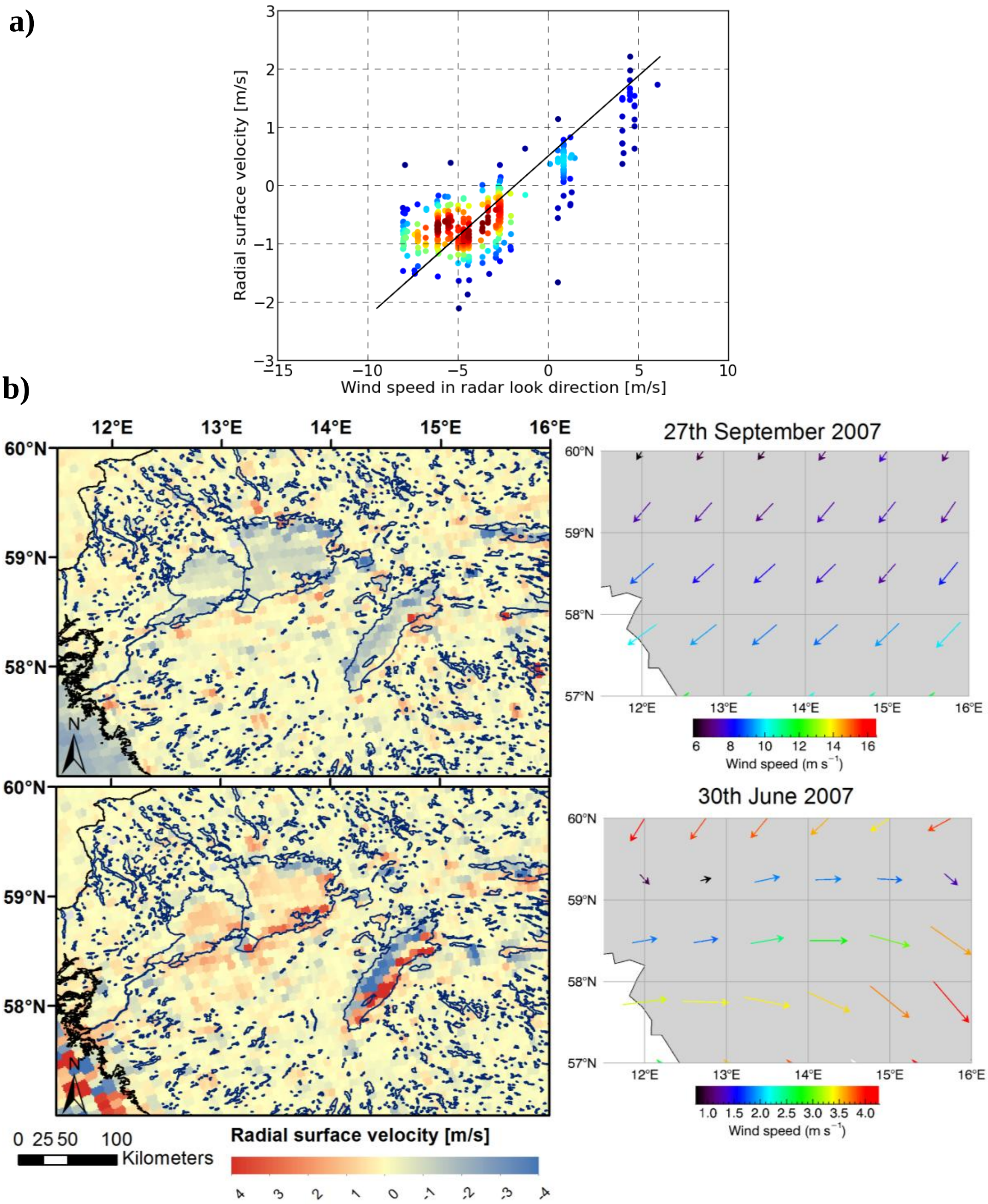


Figure 6-6: a) Scatter plot of ERA-Interim wind speed in the radar look direction and the radial surface velocity over water bodies computed over pixels covered 100% by water b) Examples of radial surface velocity data over Swedish lakes (left, blue lines represent the water bodies outlines) together with the corresponding ERA-Interim wind vectors (right).

**a)**

**b)**

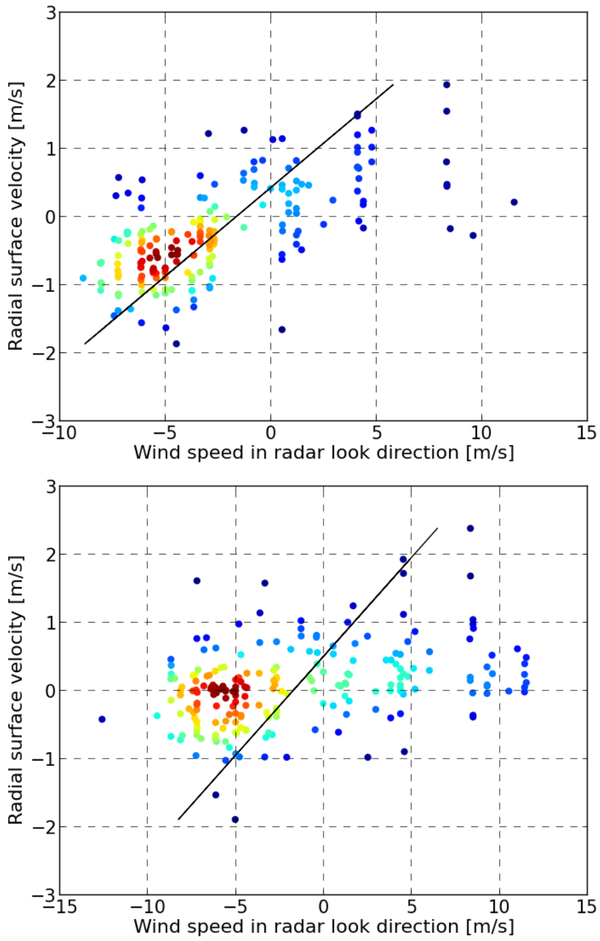


Figure 6-7: Scatter plot of ERA-Interim wind speed in the radar look direction and the radial surface velocity over water bodies computed over pixels covered a) 75 to 99% and b) 50 to 74% by water.

In case of the land contaminated water pixels, the noise increases and the relationship between radial surface velocity and wind speed becomes less pronounced (Figure 6-7). For the pixels with the water coverage between 75 and 99%, the relationship still remains relatively high ($R$=0.64, Figure 6-7 (a)). The analysis was computed from 192 data pixels that were flagged as valid by the initial mask (see chapter 5.2.1). It should be noted, these pixels are located mostly in Scandinavia. Majority of pixels over lakes Balaton and Neusiedl were flagged as invalid. High backscatter variation due to urban areas in the surroundings of these lakes hampers the retrieval of Doppler centroid anomaly. Furthermore, Balaton and Neusiedl lakes are too small to provide pixels covered by water only (see Figure 5-2). As a result the ASAR WS Doppler centroid anomaly dataset is not usable in this region.

The example of the radial surface velocity data over lakes Balaton and Neusidl is presented in Figure 6-8. High noise is apparent over the land areas, especially around larger cities (Vienna and Bratislava) and around the Balaton Lake. No significant signal difference is apparent between the land and the lakes, even though the wind speed of the selected acquisition equals to 15.6 m/s and the angle between wind direction and radar look angle is approximately 25 degrees.

Without the masking, the *R* between the ERA-Interim wind speed in the radar look direction and the radial surface velocity decreases to 0.19 for of the land/water mixed pixels covered by at least 75% by water. The *R* values than further decreases for the pixels with a water fraction between 50 and 74%. In particular, the *R* values equals to 0.35 and 0.09 in case of the masked and not-masked data respectively. The data with water pixel coverage below approximately 75% are therefore not usable for the radial surface velocity retrieval

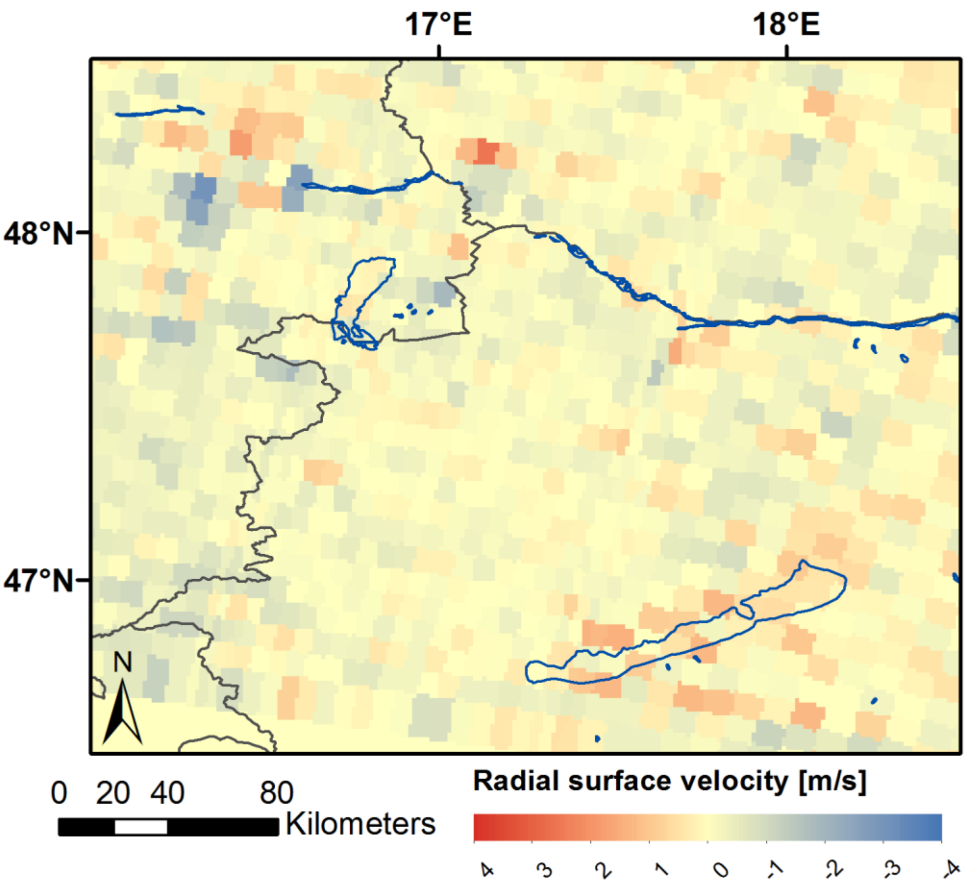


Figure 6-8: Example of radial surface velocity data over lakes Balaton and Neusiedl (blue lines represent the water bodies outlines) acquired at 09:07 on 14th October 2009

All the results are summarized in Table 6-2. The number of valid pixels compared to the number of all available pixels reveals that over inland water bodies, only about 50% of the data are suitable for the Doppler centroid anomaly estimation. This is caused predominantly by large backscatter variance or by very low NRCS values (below -20dB according to Hansen et al., 2011) within the Doppler centroid estimation area. In case of the mixed land/water pixels, this ratio is even lower – only around 20% of the pixels are flagged as valid. This is due to the errors in the measured Doppler centroid caused by the NRCS variation within the Doppler centroid estimation area. Generally, the combined limiting effect of the low spatial resolution resulting in mixed land/water pixels and the errors in the measured Doppler centroid caused by the backscatter variation within the Doppler centroid estimation area were found as the most important limiting factors for the radial surface velocity retrieval over inland water bodies.

| | **Only valid pixels** | | **All available pixels** | |
|---|---|---|---|---|
| **Class** | **Number of pixels** | ***R*** | **Number of pixels** | ***R*** |
| **Ocean pixels (100% of water)** | 34086 | 0.85 | 50399 | 0.50 |
| **Inland water bodies (100% of water)** | 413 | 0.79 | 772 | 0.51 |
| **Inland water bodies (75-99% of water)** | 192 | 0.64 | 844 | 0.19 |
| **Inland water bodies (50-74% of water)** | 214 | 0.35 | 901 | 0.09 |
| **Inland water bodies (25-50% of water)** | 1105 | 0.11 | 2551 | 0.06 |

Table 3-2: Summary of the results of the radial surface velocity analysis over water surfaces.

## 6.3 Doppler centroid anomaly data over land

The results presented in the previous chapter indicate, that the ASAR WS Doppler centroid velocity values over lakes Balaton and Neusiedl are not suitable for the radial surface velocity retrieval mainly due to the fact that only mixed land/water pixels are available. On the contrary, a linear relationship (R=0.79 in case of valid pixels covered by water only) was found between the radial surface velocity dataset and ERA-Interim wind speed in the radar look angle direction for larger lakes (> 1000 km2) located in Scandinavia. Over these lakes, the wind induced geophysical Doppler shift causes values with magnitudes up to +/-2 m/s. In this chapter, the radial surface velocity values over land are used to assess the radial surface velocity errors. Next, it is assessed if the wind induced velocity values over lakes are significantly higher than the the estimated error. It should be reiterated, that this analysis was performed using the range Doppler velocity values, i.e. the velocity values not projected to the horizontal plane.

Figure 6-9 shows the RMSE values of the range Doppler velocity for the selected ASAR WS acquisitions. The values range between 0.22 and 0.33 m/s with an exception of the image acquired on 7th May 2008 , where the RMSE equals to 0.90 m/s. However, it was found that this high value is caused by the erroneous longitude values used in the predicted Doppler centroid that impacted the last line of the image. After masking of the corrupted pixels, the RMSE is reduced to 0.33 m/s.

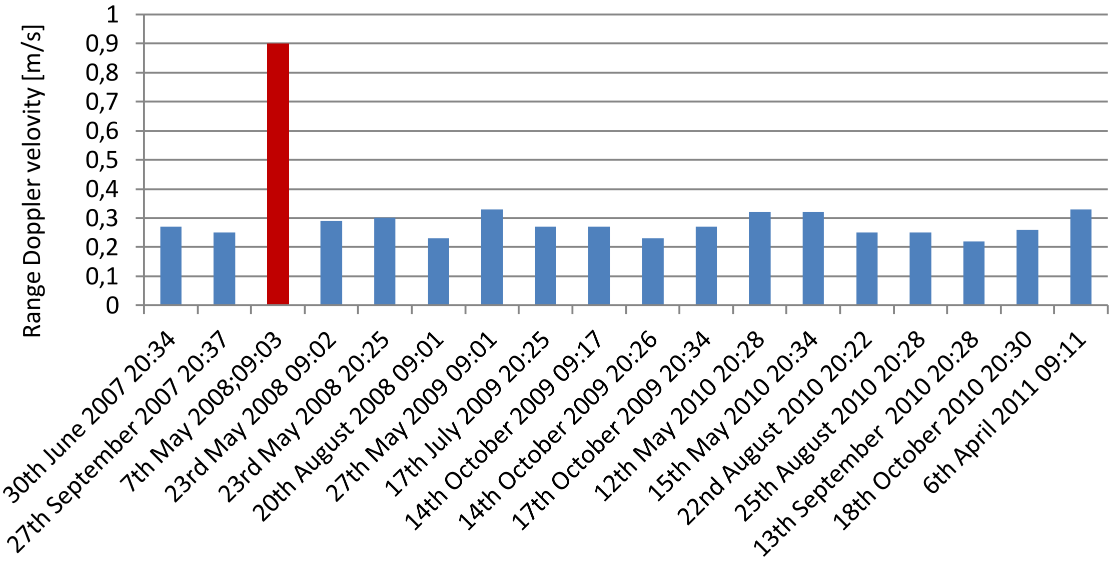


Figure 6-9: RMSE values of the range Doppler velocity datasets.

Generally, the precision of the measured Doppler centroid anomaly is expected to decrease over urban areas due to the strong backscatter variation when compared to i.e. forest or ocean areas (Li et al., 1985). The box-plot representations of the range Doppler velocity values were plotted for the forested and urban areas as well as for other land cover classes (Figure 6.10). The Corine Land Cover repository was used for the classification. The forest pixels were defined as those covered by at least 90% by forest and the urban areas as those where at least 50% of the pixel area is classified as urban areas. The spread of the velocity values is, as expected, the largest over urban areas resulting in the RMSE value of 0.59 m/s. Over forests it equals to 0.19 m/s and in other land cover classes to 0.28 m/s. The systematic difference in RMSE values correspond to that found by Hansen et al. (2011), who reported RMSE of range Doppler velocity over Amazon Forest of 0.07 m/s when compared to 0.11 to 0.13 m/s computed over all valid pixels.

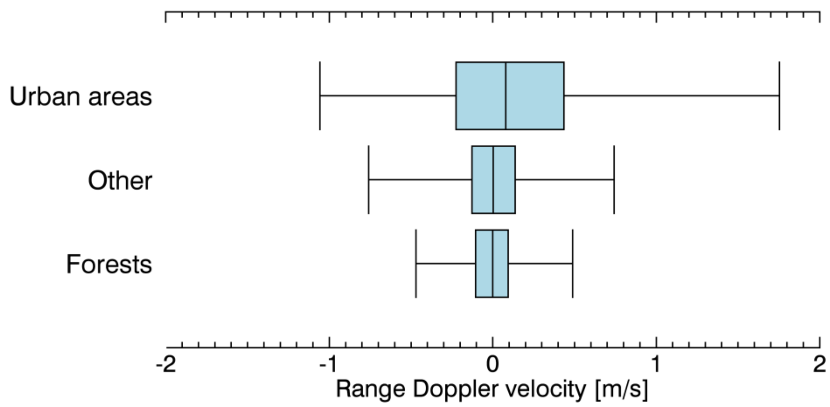


Figure 6-10: The box-plot representations of the range Doppler velocity data over Urban, Forest and Other areas. The boxes show the median, 25$^{th}$ and 75$^{th}$ percentiles; the lines represent minimum and maximum values after outlier removal (1$^{st}$ and 99$^{th}$ percentile)

The systematic influence caused by the backscatter gradients within the Doppler centroid estimation pixels was minimized by the correction of the errors in the measured Doppler centroid introduced in Chapter 4.3.1 (Hansen et al., 2011). Still, over the urban areas, outliers of extremely high values (up to 5 m/s range Doppler velocity) are present. Furthermore, similar outliers appear also over forest and agriculture areas. These are typically 4 to 8 pixels large and are located often on the same position on multiple ASAR WS acquisitions although no large variation in backscatter is apparent (Figure 6-11).

The subset of the radial surface velocity image over Scandinavia acquired on 15$^{th}$ May 2010 is presented in Figure 6-11 (a). The velocity values range between -0.5 and +0.5 m/s over most of the areas with an exception of urban areas and ocean as well as inland water and mixed land/water pixels. The values reach up to 3m/s in case of large cities (Malmö or Hamburg area) and up to 3.5m/s in case of water pixels. Outliers up to 6m/s are located at land/water boundaries due to a large backscatter gradient within the Doppler centroid estimation area in these regions (see Chapter 6.2). However the highest velocity values are located in the area around 59.60°N and 11.05°E. The values between 2.5 and 12 m/s (Figure 6-11 (b)) are located over forested and agricultural area with no apparent exceptional backscatter variation (Figure 6-11 (c) and (d)). The outliers are located at the same position on 3 different acquisitions with the same acquisition time of 20:34. The specific viewing geometry of these acquisitions most probably caused an exceptionally enhanced backscatter values (over 18 dB) from a small industrial area (Figure 6-11 (e)). Such exceptionally high values are probably caused by the roofs of the corrugated iron and appear only on under very specific viewing geometry – no outliers are apparent in images of the area acquired from a different orbit. Although the area of enhanced NRCS is relatively small, the corner reflector causes outliers in 5 surrounding Doppler centroid anomaly pixels.

As only the areas with an altitude below 200 m were selected as a reference data for the correction of the errors in the predicted Doppler centroid described in Chapter 4.3.2 (Hansen et al., 2011), the retrieval accuracy is assumed to decrease with altitude. However, apart from the pixels with very high average altitude (over 1200 m), no pronounced decrease in precision is apparent (Figure 6-12). The best results are, as expected, in the areas with altitudes below 200 m (RMSE=0.20m/s) but these only slightly differ from RMSE values for the areas with average altitude below 600 (RMSE=0.24m/s).

Based on these results, the following pixels were excluded from the further analysis:

- Pixels covered by more than 50% by urban land cover classes according to the Corine Land Cover repository
- Pixels within 10 km distance from exceptionally high backscatter values (over 15dB)
- Pixels with an average altitude over 600 m

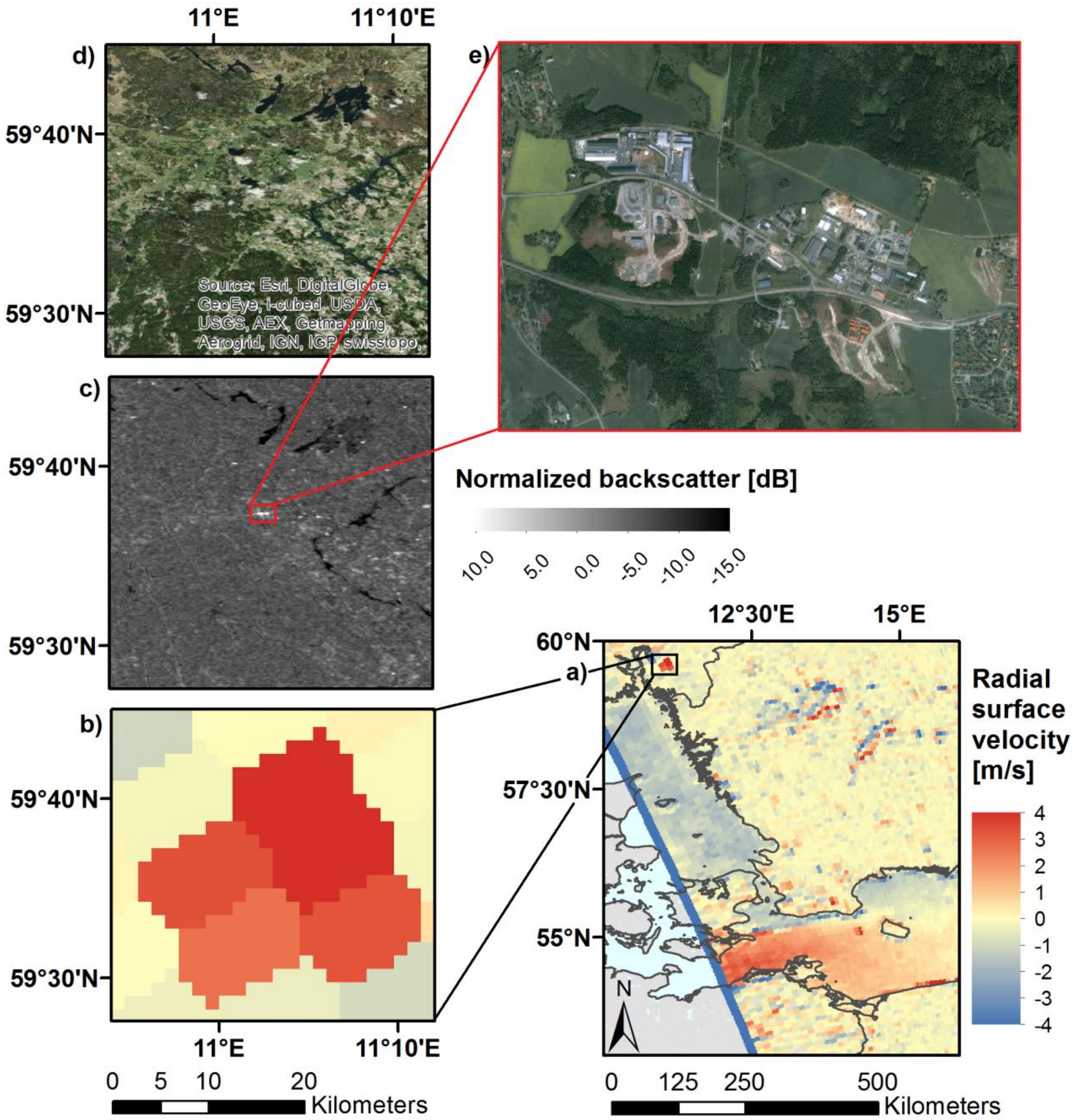


Figure 6-11: The example of a strong signal reflector causing an outlier in the radial surface velocity dataset. a): overview of the area, b) outliers up to 12 m/s in the radial surface velocity, c) NRCS image of the corresponding area, d) optical image of the corresponding area, e) group of buildings causing the enhanced backscatter over the area.

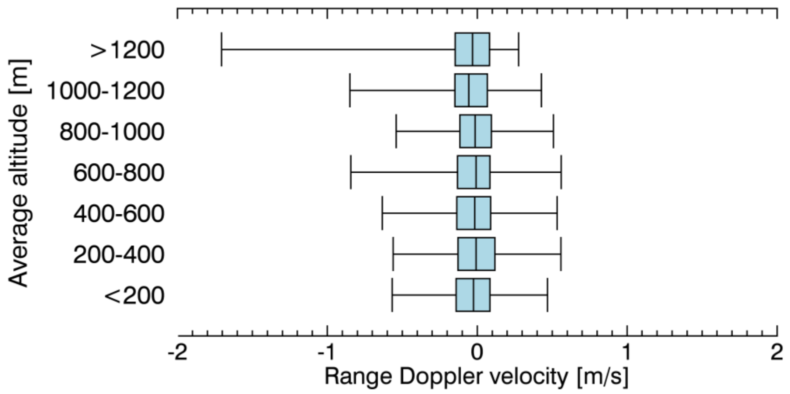


Figure 3 6-12: The box-plot representations of the range Doppler velocity data stratified according to the average altitude. The boxes show the median, 25th and 75th percentiles; the lines represent minimum and maximum values after outlier removal (1st and 99th percentile)

Figure 6-13 shows the acquisition from 15th May 2010 together with the corresponding ERA-Interim modelled wind vectors. The land areas were masked according to the rules listed above (no masking is applied for the water areas except of the masking of the land/ocean boundary). The RMSE in range Doppler velocity equals to 25cm/s after the masking (in comparison to 0.32 cm/s before the masking). This corresponds to 45cm/s range surface velocity at the incidence angle of 35°. Generally, northern part of the image is less noisy than the southern part, presumably due to a lower density of urban areas and thus higher accuracy of the measured Doppler centroid. The relative surface velocity values over Baltic Sea reach up to 3.8 m/s. Over the in-land water surfaces, a lot of outliers are apparent, especially over Vättern and Neusiedl lakes. Only in case of Lake Vänern, the velocity values correspond to the modelled wind vectors. Still most of them do not exceed the threshold of two times the RMSE value to be clearly distinguishable from noise.

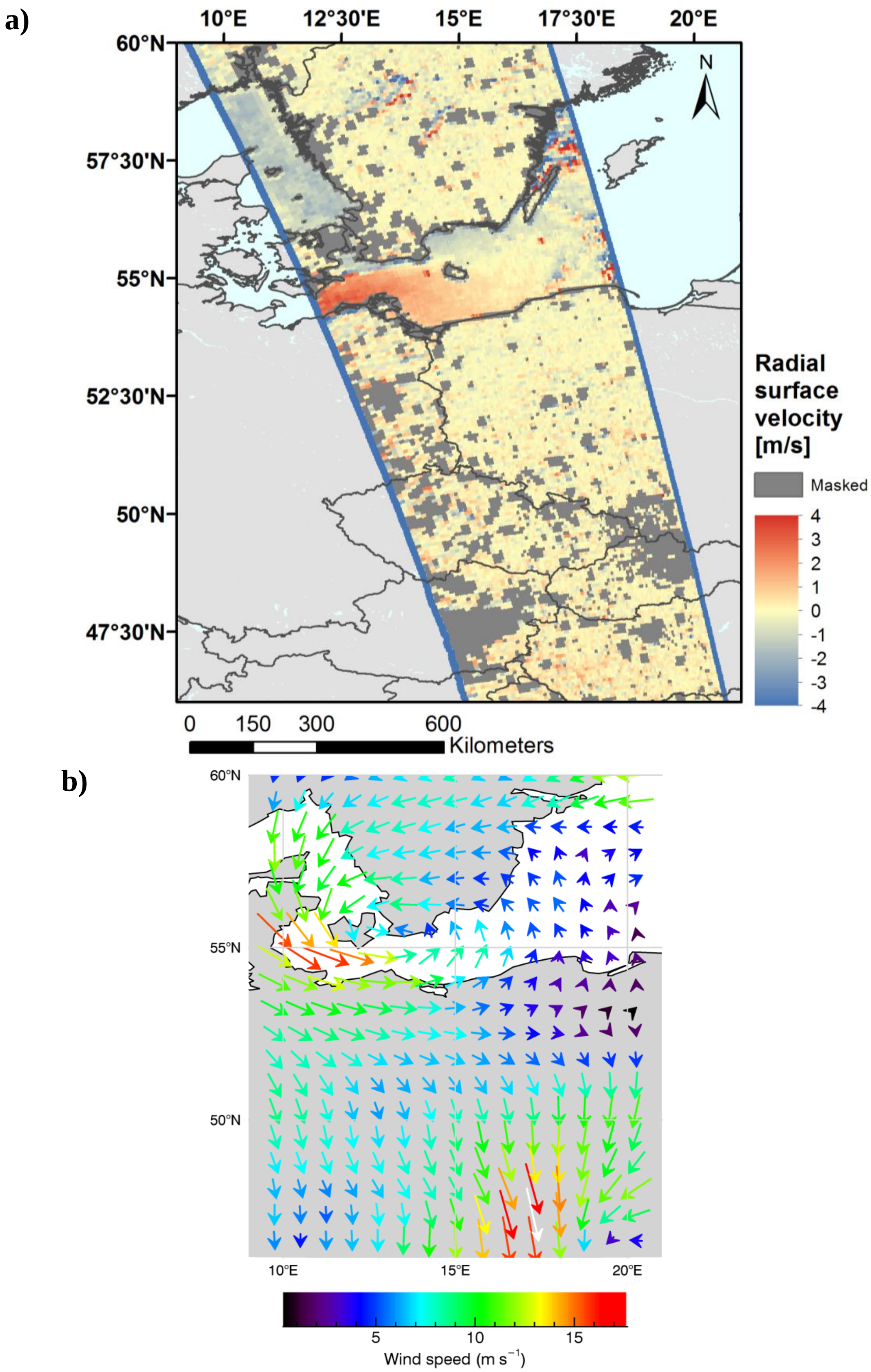


Figure 6-13: a) Masked ASAR WS radial surface velocity data acquired on 15th May 2010, b) the wind vectors over Europe from 15th May 2010 (18:00) according to the ERA-Interim model.

When computed from all 18 ASAR WS acquisitions, therange Doppler velocity RMSE equals to 24 cm/s after masking of the above described areas. This corresponds to 42 cm/s radial surface velocity at the incidence angle of 35°. As the distribution of the radial surface velocity data over land is Gaussian with an average value of 0 cm/s, the RMSE represents an estimate of a standard deviation of the data (Figure 6-13). In case of the normally distributed data, 95% of the values are expected to be within the threshold of +/- two times RMSE value. This corresponds to a radial surface velocity threshold of +/-84cm/s in case of the incidence angle of 35°.

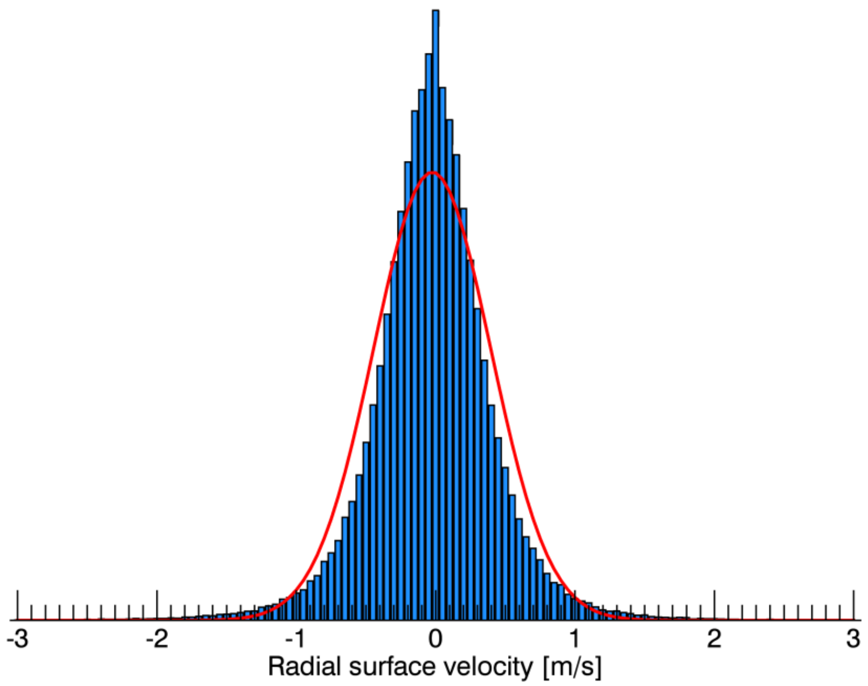


Figure 6-13: The histogram showing the distribution of the radial surface velocity data over land areas. The red line corresponds to the normal distribution data with mean value equal to 0 and standard deviation equal to the RMSE value of 42 cm/s.

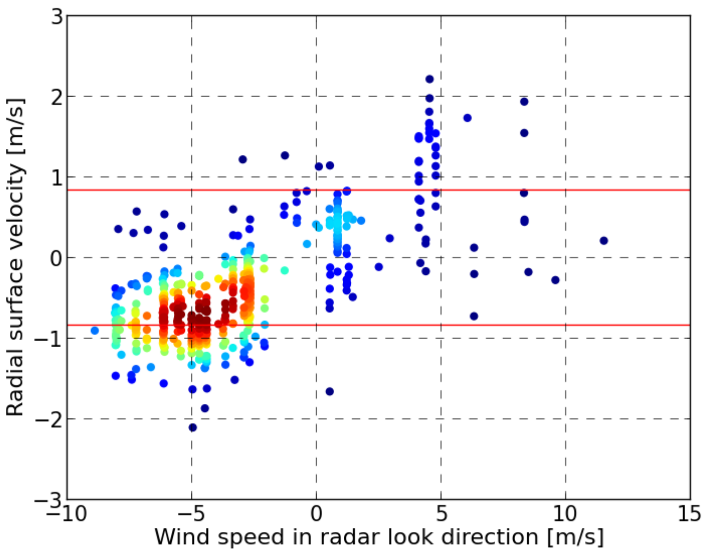


Figure 6-14: The scatter plot of radial surface velocity values and radar line of sight wind speed for inland water bodies pixels containing at least 75% of water. Red lines indicate the thresholds of two times RMSE of the radial surface velocity data over land.

As presented in Chapter 6.2, the wind induced radial surface velocity over pixels covered by at least 75% by inland water stays within the range of +/-2 m/s with most of the values below the above specified threshold of +/- 84 cm/s (see also Figure 6-14). The radial surface velocity data reach the threshold value in case of the wind speed in the radar line of sight direction of approximately 5 m/s. Average ERA-Interim wind speed in the radar line of sight direction over lakes Vännern and Vätern for the available ASAR WS acquisitions are presented in Table 6-3. Only two acquisitions - 12$^{th}$ and 15$^{th}$ May 2010 - exceed the value of 5 km/h. The threshold of 84 cm/s was applied on the corresponding radial surface velocity dataset to classify the images to water and land areas. Ocean areas were masked and excluded from the classification. The results were compared to the water map computed from the Corine Land Cover (pixels containing at least 75% of water were classified as water).

The threshold of 84 cm/s leads to strong underestimation of water areas. Only 69% of inland water pixels were classified correctly as water in case of the acquisition from 15$^{th}$ May and this number further decreases to 35% in case of the acquisition from 12$^{th}$ May. Wind induced radial surface velocity is not high enough even in case of the wind speed exceeding 6 m/s in the radar line of sight direction. Decreasing the threshold would on the other hand increase the number of pixels falsely classified as water. In case of the threshold of 84 cm/s, 5% of pixels are falsely classified as water for both acquisitions. In case of the decreasing of the threshold to 1.5 multiple of standard deviation (64 cm/s), this number increases to 10 % and the number of correctly classified water pixels increases to 79 and 63% respectively (Figure 6-15). Generally, the low retrieval accuracy of the radial surface velocity over land together with the relatively low wind speeds over inland water bodies when compared to the ocean surface hinders the usability of the ASAR WS radial surface velocity data even in case of the inland water bodies exceeding 1000 $km^2$. Even in case of the pixels covered by water only, the difference between noise and wind induces radial surface velocity is not large enough to be used for classification in any of the selected images.

| Acquisition time | Vännern Lake [m/s] | Vätern Lake [m/s] |
|---|---|---|
| **30th June 2007; 20:34:50** | 0.8 | 0.5 |
| **27th September 2007; 20:37:04** | -4.9 | -5.0 |
| **23rd May 2008; 20:25:21** | -3.9 | -5.5 |
| **17th July 2009: 20:25:54** | -2.9 | -3.1 |
| **17th October 2009; 20:34:15** | -2.8 | -3.4 |
| **12th May 2010; 20:28:15** | -6.7 | -6.7 |
| **15th May 2010; 20:34:14** | -7.8 | -6.9 |
| **22nd August 2010; 20:22:53** | 4.9 | 4.4 |

Table 6-3: the average wind speeds for available ASAR WS radial surface velocity acquisitions over Swedish lakes Vännern and Vätern

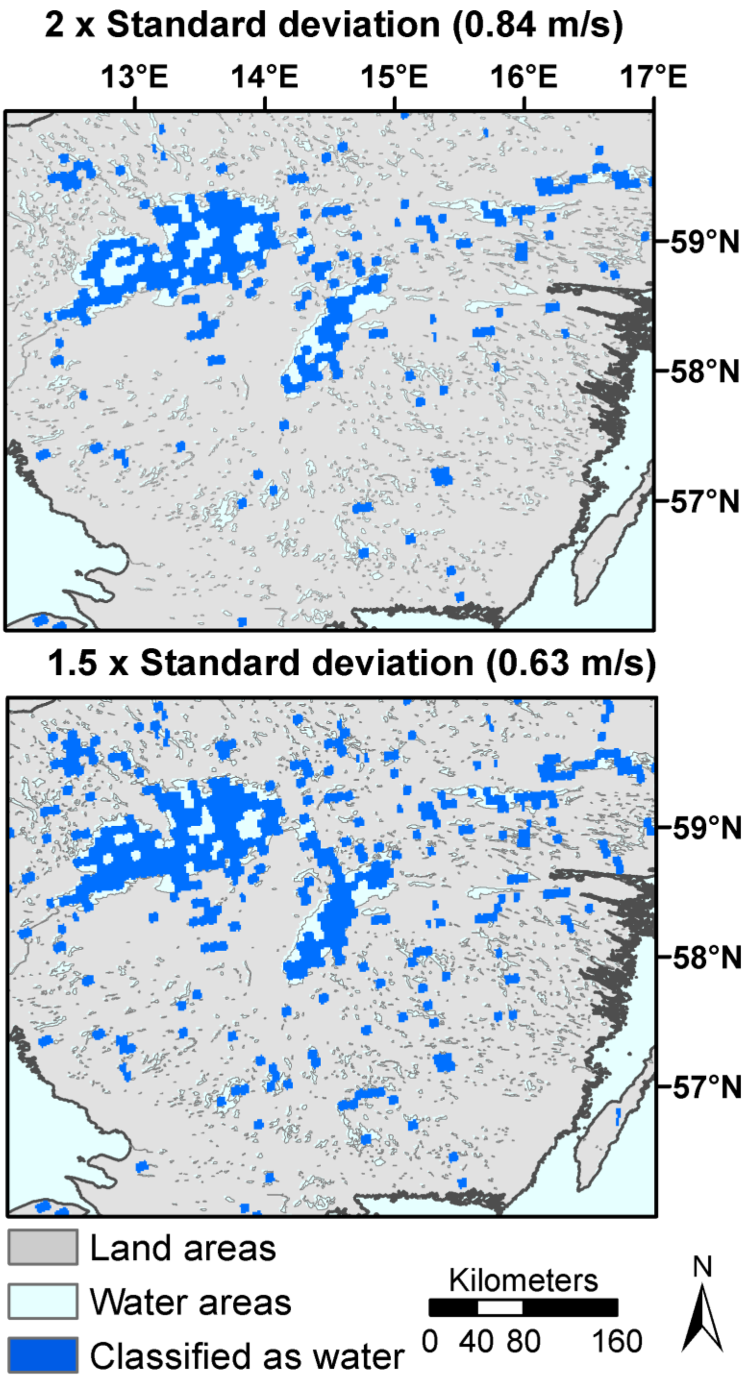


Figure 6-15: Results of a threshold based classification of the radial surface velocity data over southern Sweden for the acquisition from 15th May 2010. Pixels classified as water are highlighted in blue. Up: threshold of 2 x RMSE, Down: threshold of 1.5 x RMSE.

# Chapter 7

## Summary and outlook to Sentinel 1

With their fine spatial resolution and practically all-weather measuring capability, the SAR systems are increasingly important for the mapping of water surfaces. Variety of methods were developed over last decades, however most of them have restrictions over rough water surfaces. High wind speeds and water currents enhance the SAR backscatter from the water surface and hinder the water detection traditionally based on an assumption of low backscatter response from the water surface.

Within this thesis, a complementary dataset derived from SAR data - a Doppler centroid anomaly information - was analysed and tested for its applicability for the water surface mapping. The Doppler centroid anomalies computed from Envisat ASAR WS data were converted to radial surface velocities that express the measure of the relative velocity of the surface towards or from the satellite. According to the theory, this velocity is equal or very close to zero for any stable Earth surface and increases or decreases in case of the moving water surface. Water currents or near-surface winds are reflected in the radial surface velocity data, which has already been successfully used in SAR oceanography (Wang et al., 2014 or Johannessen et al., 2014). Within this thesis, the $R$ between the wind speed in the direction of the radar line of sight and the radial surface velocity data over the Baltic Sea was found to be equal to 0.85.

Relationship between the wind speed in the direction of the radar line of sight and the radial surface velocity values was confirmed also for large Scandinavian lakes (over 1000km$^2$) expressed by the $R$ of 0.79 and 0.64 in case of the water only pixels and mixed pixels containing at least 75% of water respectively. The increasing wind speed in the direction close to the radar line of sight direction increases the SAR backscatter from the water surface and therefore hinders the water surface detection in the SAR images. However, it is also reflected in the radial surface velocity value over the area which is the most important precondition for the usage of this data for the mapping of the inland water.

Due to significantly lower wind speeds over land surface when compared to the oceans, the variability of the radial surface velocity data over inland water bodies is limited when compared to those over Baltic Sea. The highest radar line of sight wind speeds within the selected acquisitions were equal to 8 m/s in case of the Swedish lakes, whereas over the Baltic Sea, the wind speeds ranged up to 20 m/s. Due to the relatively low range of the radial surface velocity data over inland water bodies, the retrieval accuracy of the Doppler centroid anomaly is an important issue.

According to the accuracy assessment performed by Hansen et al. (2011), the RMSE of the range Doppler velocity equals to 13 and 11cm/s for the VV and HH polarisation respectively for the data below 200m altitude and with the mask containing the data proximal to land/ocean border, data with large backscatter gradients within the Doppler centroid estimation pixels and data exceeding three times the RMSE. To assess the retrieval accuracy without these strict limitations, the RMSE was computed for all land pixels and less conservative mask was created based on the results. The resulting RMSE was found to be equal to 24 cm/s and the following rules were used for the masking:

- Pixels covered by more than 50% by urban land cover classes according to the Corine Land Cover repository
- Pixels within 10 km distance from exceptionally high backscatter values (over 15dB)
- Pixels with an average altitude over 600 m

The most obvious limiting factor of the radial surface velocity dataset is its limited spatial resolution. In case of Envisat ASAR, the available spatial resolution equals to 3.5 to 9 km in range direction and 8 km in azimuth direction which limits the applicability of the current datasets to very large water bodies only. Even in case of lakes with an area between 300 and 1000km$^2$, the proximity to land and presence of bright targets within the Doppler centroid estimation area biases the Doppler centroid anomaly values. The radial surface velocity values over lakes Balaton and Neusiedl (area of 592 and 315 km$^2$ respectively) were found to contain no relevant information about the water surface velocity as they do not reflect the near surface wind conditions.

Furthermore, the retrieval accuracy was also found to be an important limitation of the current Envisat ASAR data. In spite of the $R$ of 0.79 between full water pixels and radar line of sight wind speed, the radial surface velocities over lakes Vännern and Vätern (area of 5655 and 1893 km$^2$ respectively) were not high enough to allow the specification of a threshold that would clearly delineate the water and land areas on any of the selected acquisitions. The threshold of 1.5 and 2 times the RMSE was applied on two selected scenes with the highest radar line of sight wind speeds over Scandinavia. Even in case of the lower threshold, the water areas were underestimated (63 and 79% water pixels were correctly classified as water in case of the acquisitions from 12$^{th}$ and 15$^{th}$ May 2010 respectively when using the lower threshold). The conclusion based on the presented results is, that with the current retrieval accuracy of the ASAR WS Doppler centroid anomaly data, the radial surface velocity information is not usable over the land areas for the water surface detection. To consider the data from the future sensors, not only the spatial resolution, but also the retrieval accuracy needs to be improved significantly.

The radial surface velocity data will be a part of the Level 2 ocean product of the recently launched Sentinel-1 satellite. The requirements from the user community concerning the Sentinel-1 data include the spatial resolution of 1x1km and the retrieval accuracy better than 10 cm/s (Engen et al., 2014). This accuracy is not achieved by the current time domain Doppler estimator based on the Madsen algorithm (Madsen et al., 1989) that is currently used for the ASAR WS data and was therefore used also within the scope of this thesis. Therefore, new Doppler estimation algorithm was proposed and evaluated with the help of the ASAR data over coastal areas and rain forest by Engen et al. (2014).

The accuracy of 3.81 and 2.55 Hz was achieved for the coastal ocean and rain forest respectively, which corresponds to the range Doppler velocity of 11 and 7 cm/s for the data with spatial resolution of 2x2km. Within this thesis, the accuracy of the range Doppler velocity over forested areas was found to be 19 cm/s in case of the spatial resolution 8x3.5 to 9km. The new methodology is therefore expected to provide an improvement both in the spatial resolution as well as in the retrieval accuracy. The Sentinel-1 Interferometric Wide swath mode is expected to provide comparable performance results to those presented by Engen et al. (2014).

In case of the current ASAR WS range Doppler velocity dataset presented in this thesis, the retrieval accuracy varies strongly between the forested areas and other land cover classes (RMSE of 59 cm/s over urban areas when compared to 19 cm/s over forests). The results presented by Engen et al. (2014) over rain forests and coastal areas are promising, as both the spatial resolution as well as the retrieval accuracy are expected to improve in case of the Sentinel-1 radial surface velocity. Nevertheless, its usability for the water surface mapping can be assessed only after the evaluation of the retrieval accuracy over all land cover classes.

# Bibliography

Atlas, R., Hoffman, R. N., Ardizzone, J., Leidner, S. M., Jusem, J. C., Smith, D. K., & Gombos, D. (2011). A cross-calibrated, multiplatform ocean surface wind velocity product for meteorological and oceanographic applications.*Bulletin of the American Meteorological Society*, *92*(2), 157-174.

Bates, P. D., Horritt, M. S., Smith, C. N., & Mason, D. (1997). Integrating remote sensing observations of flood hydrology and hydraulic modelling.*Hydrological Processes*, *11*(14), 1777-1795.

Bossard, M., Feranec, J., & Otahel, J. (2000). CORINE land cover technical guide: Addendum 2000.

Chapron, B., Collard, F., & Ardhuin, F. (2005). Direct measurements of ocean surface velocity from space: Interpretation and validation. *Journal of Geophysical Research: Oceans (1978–2012)*, *110*(C7).

Chelton, D. B., Schlax, M. G., Freilich, M. H., & Milliff, R. F. (2004). Satellite measurements reveal persistent small-scale features in ocean winds. *Science*,*303*(5660), 978-983.

Curlander, J.C. & McDonough, R.N.; *Synthetic Aperture Radar — Systems and Signal Processing*. Hoboken, NJ:Wiley, 1991, Wiley series in Remote Sensing.

Dagestad, K. F., Horstmann, J., Mouche, A., Perrie, W., Shen, H., Zhang, B., ... & Vachon, P. (2012). Wind retrieval from synthetic aperture radar-an overview. In *4th SAR Oceanography Workshop (SEASAR 2012)*.

Dee, D. P., Uppala, S. M., Simmons, A. J., Berrisford, P., Poli, P., Kobayashi, S., ... & Vitart, F. (2011). The ERA-Interim reanalysis: Configuration and performance of the data assimilation system. *Quarterly Journal of the Royal Meteorological Society*, *137*(656), 553-597.

Engen, G., Johnsen, H., & Larsen, Y. (2014). Sentinel-1 Geophysical Doppler Product-Performance and Application. In *EUSAR 2014; 10th European Conference on Synthetic Aperture Radar; Proceedings of* (pp. 1-4). VDE.

*ENVISAT, A. S. A. R. product Handbook* (2007). European Space Agency.

Giustarini, L., Hostache, R., Matgen, P., Schumann, G. P., Bates, P. D., & Mason, D. C. (2013). A change detection approach to flood mapping in urban areas using TerraSAR-X. *Geoscience* *and Remote Sensing, IEEE Transactions on*, *51*(4), 2417-2430.

Gleick, P. H., 1996: Water resources. In Encyclopedia of Climate and Weather, ed. by S. H. Schneider, Oxford University Press, New York, vol. 2, pp.817-823.

Greifender, F. (2012),*Towards an Automated SAR-Based Classification of Water Bodies*, (Master's Thesis)

Hahmann, T., Roth, A., Martinis, S., Twele, A., & Gruber, A. (2008, July). Automatic extraction of water bodies from TerraSAR-X data. In *Geoscience and Remote Sensing Symposium, 2008. IGARSS 2008. IEEE International*(Vol. 3, pp. III-103). IEEE.

Hansen, M.W. (2011), *Sea Surface Range Doppler Velocity Retrievls from Synthetic Aperture Radar*, (Doctoral dissertation)

Hansen, M. W., Collard, F., Dagestad, K., Johannessen, J. A., Fabry, P., & Chapron, B. (2011). Retrieval of sea surface range velocities from Envisat ASAR Doppler centroid measurements. *Geoscience and Remote Sensing, IEEE Transactions on*, *49*(10), 3582-3592.

Jin, M. Y. (1996). Optimal range and Doppler centroid estimation for a ScanSAR system. *Geoscience and Remote Sensing, IEEE Transactions on*,*34*(2), 479-488.

Johannessen, J. A., Chapron, B., Collard, F., Raj, R., Hansen, M., & Tournadre, J. (2014, June). Range Doppler centroid shift-altimetry comparison. In *EUSAR 2014; 10th European Conference on Synthetic Aperture Radar; Proceedings of* (pp. 1-3). VDE.

Li, F. K., Held, D. N., Curlander, J. C., & Wu, C. (1985). Doppler parameter estimation for spaceborne synthetic-aperture radars. *Geoscience and Remote Sensing, IEEE Transactions on*, (1), 47-56.

Liebe, J. R., van de Giesen, N., Andreini, M. S., Steenhuis, T. S., & Walter, M. T. (2009). Suitability and limitations of ENVISAT ASAR for monitoring small reservoirs in a semiarid area. *Geoscience and Remote Sensing, IEEE Transactions on*, *47*(5), 1536-1547.

Liu, H., & Jezek, K. C. (2004). Automated extraction of coastline from satellite imagery by integrating Canny edge detection and locally adaptive thresholding methods. *International Journal of Remote Sensing*, *25*(5), 937-958.

Madsen, S. N. (1989). Estimating the Doppler centroid of SAR data. *Aerospace and Electronic Systems, IEEE Transactions on*, *25*(2), 134-140.

Martinis, S., Twele, A., & Voigt, S. (2009). Towards operational near real-time flood detection using a split-based automatic thresholding procedure on high resolution TerraSAR-X data. *Natural Hazards and Earth System Science*, *9*(2), 303-314.

Matgen, P., Hostache, R., Schumann, G., Pfister, L., Hoffmann, L., & Savenije, H. H. G. (2011). Towards an automated SAR-based flood monitoring system: Lessons learned from two case studies. *Physics and Chemistry of the Earth, Parts A/B/C*, *36*(7), 241-252.

Mouche, A. A., Collard, F., Chapron, B., Dagestad, K., Guitton, G., Johannessen, J. A., ... & Hansen, M. W. (2012). On the use of Doppler shift for sea surface wind retrieval from SAR. *Geoscience and Remote Sensing, IEEE Transactions on*, *50*(7), 2901-2909.

Nilsson, C. S., & Tildesley, P. C. (1995). Imaging of oceanic features by ERS 1 synthetic aperture radar. *Journal of Geophysical Research: Oceans (1978–2012)*, *100*(C1), 953-967.

Otsu, N. (1975). A threshold selection method from gray-level histograms.*Automatica*, *11*(285-296), 23-27.

Provost, F., & Kohavi, R. (1998). Guest editors' introduction: On applied research in machine learning. *Machine learning*, *30*(2), 127-132.

Raney, R. K. (1986). Doppler properties of radars in circular orbits. *International Journal of Remote Sensing*, *7*(9), 1153-1162.

Rouault, M. J., Mouche, A., Collard, F., Johannessen, J. A., & Chapron, B. (2010). Mapping the Agulhas Current from space: An assessment of ASAR surface current velocities. *Journal of Geophysical Research: Oceans (1978–2012)*, *115*(C10).

Sabel, Daniel. *ENVISAT ASAR Processing at IPF*.

Schultz, Gert A. *Remote sensing in hydrology and water management*. Vol. 1. Berlin etc.: Springer, 2000.

Schumann, G., Bates, P. D., Horritt, M. S., Matgen, P., & Pappenberger, F. (2009). Progress in integration of remote sensing–derived flood extent and stage data and hydraulic models. *Reviews of Geophysics*, *47*(4).

Davis, Shirley M., et al. "Remote sensing: the quantitative approach." *New York, McGraw-Hill International Book Co., 1978. 405 p.* 1 (1978).

Ulaby, F. T., Moore, R. K., & Fung, A. K. (1982). Microwave Remote Sensing Active and Passive-Volume II: Radar Remote Sensing and Surface Scattering and Emission Theory.

Vachon, P. W. & Wolfe, J. (2011). C-band cross-polarisation wind speed retrieval, *IEEE Geocsi. Remote Sens. Lett.*, 8, 456-459.

van Dijk, A. I. J. M., Renzullo, L. J., Wada, Y., & Tregoning, P. (2014). A global water cycle reanalysis (2003–2012) merging satellite gravimetry and altimetry observations with a hydrological multi-model ensemble. *Hydrology and Earth System Sciences*, *18*(8), 2955-

2973.

Verhoef, A., Portabella, M., & Stoffelen, A. (2012). High-resolution ASCAT scatterometer winds near the coast. *Geoscience and Remote Sensing, IEEE Transactions on*, *50*(7), 2481-2487.

Wang, L., Zhou, Y., Ge, J., Johannessen, J. A., & Shen, F. (2014). Mapping sea surface velocities in the Changjiang coastal zone with advanced synthetic aperture radar. *Acta Oceanologica Sinica*, *33*(11), 141-149.

**Internet:**

JAXA Earth Observation Research Center, High resolution ocean surface wind measurement, retrieved from: http://www.eorc.jaxa.jp/ALOS/en/img_up/pal_090123.htm

http://earth.esa.int/applications/data_util/SARDOCS/spaceborne/Radar_Courses/Radar_Course_II/bragg_scattering.htm

Engen, G. & Johnsen, H. (2010); *Sentinel-1 Doppler and Ocean Radial Velocity (RVL) Algorithm Definition*, retrieved from: https://earth.esa.int/documents/247904/349449/S1_L2_RVL_AlgoDef_v1+2.pdf/a32559dd-2ce1-4663-a1d9-33e2fe764b44?version=1.1

U.S. Climate Prediction Center, updated half-yearly: CPC Global Summary of Day/Month Observations, 1979-continuing. Dataset ds512.0 published by the CISL Data Support Section at the National Center for Atmospheric Research, Boulder, CO, available online at http://dss.ucar.edu/datasets/ds512.0/.